IOWA STATE UNIVERSITY
Digital Repository

2013

Damage detection and characterization of fiber-reinforced composites using ultrasonics

Ajith Subramanian
Iowa State University

Damage detection and characterization of fiber-reinforced composites using ultrasonics

by

Ajith Subramanian

A thesis submitted to the graduate faculty

in partial fulfillment of the requirements for the degree of

MASTER OF SCIENCE

Major: Engineering Mechanics

Program of Study Committee:

Vinay Dayal, Major Professor

Daniel J. Barnard

Thomas J. Rudolphi

Michael R. Kessler

Iowa State University

Ames, Iowa

2013

TABLE OF CONTENTS

LIST OF TABLES

LIST OF FIGURES

ACKNOWLEDGEMENTS

x

ABSTRACT

Due to the prevalence of fiber-reinforced composites in industrial applications, the need for damage-detection and characterization has increased. Ultrasonic nondestructive testing (NDT) is a powerful and non-invasive method of detecting flaws and defects in composite materials. Air-coupled and immersion UT techniques are used to quantify the effect of matrix microcracking and delamination within the composite laminate. Detection of matrix microcracks in the laminate is of primary concern since microcracking is one of the initial damage modes resulting in local stiffness reduction. The techniques considered include pulse-echo in immersion, angle-beam through-transmission Lamb wave time-of-flight shift and velocity measurements, and angle-beam backscatter measurements from single microcracks within the composite laminate. The time-of-flight measurements are shown to be a reasonable method for quantifying stiffness reduction in the laminate, however special attention must be provided to the Lamb modes considered and their sensitivity to the independent stiffness components. The angle-beam backscatter technique may be used to detect individual microcracks but poses a limitation on the frequency and depth of inspection. Ultimately, the quantification of microcracking will provide an early descriptor of failure in the laminate.

CHAPTER 1.   INTRODUCTION

1.1   Background

Fiber-reinforced composites have seen widespread usage in the military, aviation, and automotive industries, to name a few. A fiber-reinforced composite laminate is typically comprised of several layers, or plies, within which there are two constituents: the fiber and matrix. Common fiber/matrix combinations include carbon/epoxy and fiberglass/epoxy composites. These composites boast superior strength-to-weight ratios and the ability to tailor the structure's material properties by using arbitrary fiber directions and ply stacking sequences.

The damage behavior of composites is complex due to their inherent anisotropy and non-homogeneity, which presents a challenge in detecting defects using standard nondestructive techniques that are used to inspect isotropic media. Damage in a composite can be categorized by both the micro and macroscopic scales, and damage modes include matrix microcracking, delamination, and fiber-breakage. The opaque nature of carbon fiber reduces the effectiveness of visual inspection, whereas the translucency of fiberglass permits visual inspection under natural conditions.

Various nondestructive testing (NDT) modalities, such as X-ray CT, thermography, ultrasonics, acoustic emission, etc., have been used to detect and identify damage types in composites. Over the last 20-30 years, there has been significant work performed in experimental ultrasonic testing to detect and characterize damage modes in composites [1–4]. This thesis will consider the inspection of carbon/epoxy laminates containing various damage morphologies using non-contact ultrasonic testing techniques such as water-coupled immersion and air-coupled

ultrasound.

1.2 Damage Modes

1.2.1 Matrix Microcracking

A matrix microcrack in a unidirectional-ply fiber/matrix composite laminate is defined as a crack whose length is confined to the ply thickness and whose depth is in the direction of the fibers in the ply. This definition may also be extended to ply-groups (i.e., multiple adjacent plies of the same fiber direction). A micrograph of a carbon/epoxy laminate containing a matrix microcrack induced by thermal fatigue is shown in Figure 1.1. In this micrograph, the thickness of the middle ply-group is approximately 1 mm. Matrix microcracking is also considered as a precursor to macroscopic failure modes [5–7].
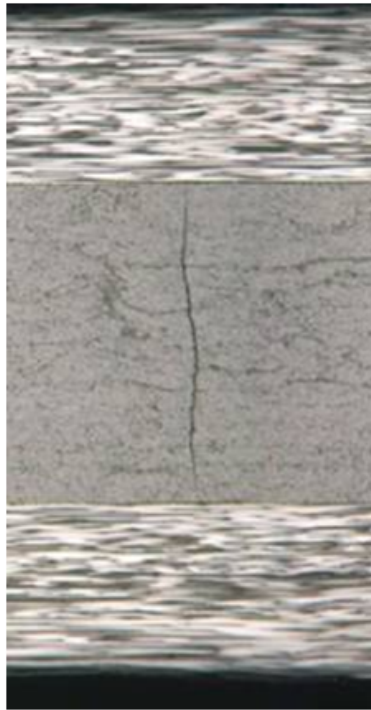
Figure 1.1: Cross-sectional micrograph of a $[0_4/90_4]_S$ IM7/8552 carbon/epoxy laminate containing a matrix microcrack induced by thermal fatigue within a ply-group of eight 90° plies

Matrix microcracking is formed due to tension stresses within the ply transverse to the fiber direction and is the primary damage mode for uniaxial tension, thermal shock, and low-energy impact. Microcracking is difficult to detect in a composite specimen using conventional ultrasonic methods such as normal incidence pulse-echo scanning due to its orientation with respect to the incident beam. The crack surface plane lies parallel to the beam direction and so there is minimal scattering from the flaw.

1.2.2 Delamination

Delamination in a fiber/matrix composite laminate is caused by interlaminar shear stresses and is defined by a crack that propagates within the "resin-rich" region between plies. Figure 1.2 shows a micrograph of a delamination between two adjacent plies.
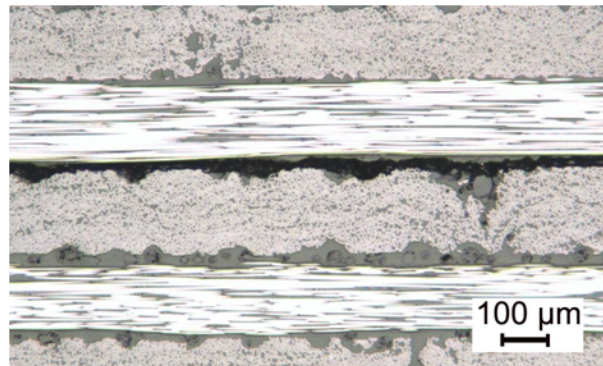
Figure 1.2: Cross-sectional micrograph of a cross-ply carbon/epoxy laminate containing a delamination

In contrast to matrix microcracking, delamination can be detected using a wide array of ultrasonic testing methods. Furthermore, delamination depth can be found using time-of-flight measurements, although delamination in lower plies are "shadowed" by the delamination in upper plies. The projected damage area can be determined from either normal incidence pulse-echo or through-transmission scanning.

1.3 Ultrasonic Testing

An ultrasonic transducer emits a high-frequency beam of sound which passes through a sample and is collected in reflection (pulse-echo), on the opposite side of the sample (through-transmission), or on the same side as the transmitting transducer (pitch-catch). Ultrasonic transducers require a coupling medium to transfer sound to the material. Coupling media include gels, oils, and water. Air-coupled transducers benefit from the lack of a couplant needed to transfer sound into the material but are limited to frequencies below 1-2 MHz due to the rapid increase of sound attenuation in air past this frequency range. However, air-coupled transducers are well-adapted to field scanning and large material geometries.

Data is collected in the form of A-scans, B-scans, and C-scans. An A-scan represents ultrasonic energy as a function of time at a single point, a B-scan represents a trace of A-scans along a single spatial dimension, and a C-scan represents a two-dimensional scan that contains an A-scan at each point. A schematic of the three different types of data representation is shown in Figure 1.3. The "t" axis represents time and the "x" and "y" axes represent spatial dimensions of the scan. For a normal-incidence scan, the time of flight is directly proportional to the depth in the material.

(a) A-scan   (b) B-scan   (c) C-scan
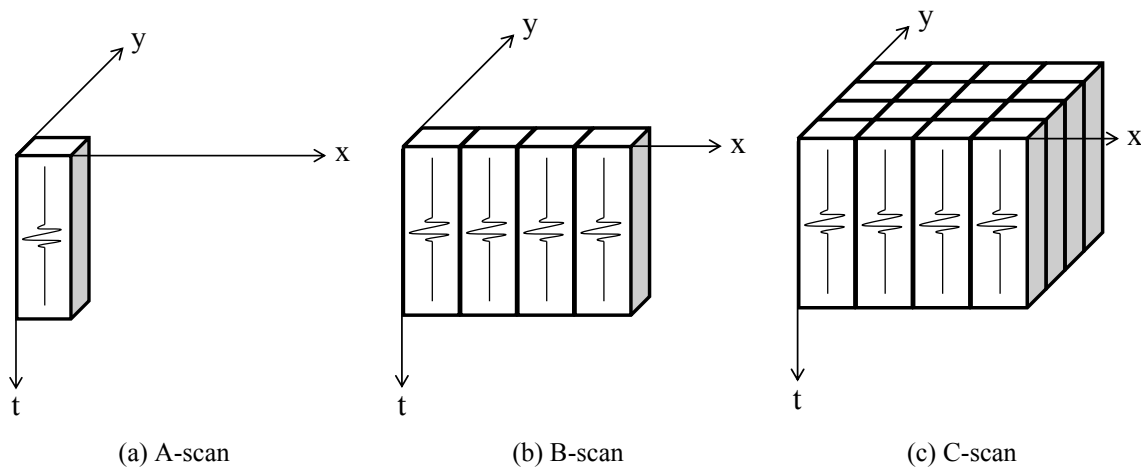
Figure 1.3: Types of UT data representation

1.4   Thesis Organization

Chapter 2 deals with impact damage in carbon/epoxy laminates and the dependence of the incident impact energy on the damage mode. In Chapter 3, air-coupled Lamb wave scans are performed on samples containing matrix microcracks. Time-of-flight (TOF) shifts are calculated over the scan distance to gauge the change in phase and group velocity within the composite laminate. X-ray MicroCT data is used to find the microcrack density along the length of the laminate and relationships are drawn between the microcrack distribution and UT results. Chapter 4 deals with angle-beam backscatter measurements from microcracks in composites, allowing for detection of single transverse cracks in a lamina or ply group. Chapter 5 contains methods used in the previous chapters with application to low-energy impacts on a solid laminate. Finally, Chapter 6 contains general conclusions and also includes comments on future work to be performed in damage detection and characterization of fiber/matrix composites.

CHAPTER 2.   DAMAGE CHARACTERIZATION OF CARBON/EPOXY LAMINATES USING COMPRESSION-AFTER-IMPACT (CAI) AND ULTRASONIC NDE

A paper published in *Review of Progress in Quantitative Nondestructive Evaluation*

A. Subramanian[1], V. Dayal[2], and D. J. Barnard[1]

[1]CNDE, Iowa State University, Ames, IA 50011

[2]Department of Aerospace Engineering, Iowa State University, Ames, IA 50011

2.1   Abstract

A study of impact damage morphology in unidirectional carbon/epoxy laminates was performed. A "load drop" method was investigated for prediction of the delamination threshold energy (E_{DT}) for impact. The impacted samples were subjected to uniaxial, in-plane compression to observe the growth of damage, failure modes, and residual strength. Samples were scanned before and after CAI using air-coupled through-transmission ultrasound and amplitude C-scans were collected for visual inspection of damage.

2.2   Introduction

The necessity to characterize damage within composite laminates has grown with their increased application in the aviation industry. Out-of-plane impact loads are one of the most common ways by which damage is introduced within a composite structure during usage. Low-

velocity impacts of this nature occur frequently during the service and maintenance of aircraft (e.g. impacts due to dropped tools) and produce visually undetectable localized damage. The two primary damage modes in fiber composites during an impact event are microcracking and delamination [8]. The damage modes can be parameterized by an impact energy threshold, or the delamination threshold energy (E_{DT}) [9]. Microcracking occurs at energies below E_{DT} and microcracking and delamination occur at energies above E_{DT}. Previous work in the area has shown that there is a local maximum in the load-time impact history that corresponds to the minimum applied load at which delamination occurs within the sample [10, 11].

Compression after impact (CAI) is a standardized method used to characterize the stiffness and strength loss in a laminate due to an impact event. An impacted sample is placed under uniaxial compression in a fixture with simple supports on all four edges. Experiments have shown that catastrophic shear failure typically occurs in the form of a crack originating from the impact location and propagating laterally towards the outer edges of the sample [12].

In this paper, unidirectional carbon/epoxy samples were subjected to out-of-plane impact loads using an instrumented drop tower. The "load drop" in the load-time history was recorded over various impact energies. The usual procedure to determine E_{DT} is performed by impacting a sample over a series of successively increasing or decreasing energies and evaluating the local impact region for indications of delamination after each impact (e.g. using ultrasonic contact probes and collecting A-scans). If E_{DT} can be calculated with reasonable accuracy from a single incident energy that produces delamination, the aforementioned trial-and-error process could be eliminated thus reducing the number of samples required. Following the impact tests, the sample was placed under uniaxial compression to obtain the stiffness and strength of the impacted samples. Both the impact test and CAI were performed using ASTM standards D 7136 and D 7137 respectively. All the tested samples were scanned using air-coupled through-transmission ultrasound and their amplitude C-scans were investigated to detect the onset of delamination and other defects.

2.3 Impact Damage

2.3.1 Sample and Drop-Tower Specifications

Two sets of laminates were fabricated using carbon/epoxy laminas. The first set consisted of "industry quality" samples (denoted by the prefix "N") with a quasi-isotropic stacking sequence and a laminate thickness of 3.53 mm. These samples contain a woven layer on the top and bottom surfaces (see Fig. 3). The second set of samples (denoted by the prefix "HM") was fabricated using IM7/8552 unidirectional prepreg, has a quasi-isotropic stacking sequence of $[+45/0/-45/90]_{4S}$, and a cured laminate thickness of 4.24 mm. Both sets of samples were cut to 101.6 mm x 152.4 mm (4 in. x 6 in.) plates such that the 0° fiber direction is along the shorter edge of the sample.

An Instron Dynatup 8200 drop-tower was used to impact the samples. A hemispherical steel impactor ("tup") with a tip diameter of 15.9 mm (0.625 in.) was used. Force readings were collected during the impact from a load cell on the impactor. The overall mass of the carriage containing the tup and weights is 5.45 kg. Furthermore, a velocity detector was used to record velocity just prior to impact. The sample was placed directly on an aluminum base plate and centered with the impactor axis over a 76.2 mm x 127 mm (3 in. x 5 in.) rectangular cutout in the base plate. The sample was restrained during impact using four toggle clamps, one at each corner of the sample. The drop-tower configuration is shown in Figure 2.1.

The impact energy guaranteed to produced delamination (E_{delam}) within the sample is calculated using Eq. 2.1. In this equation, C_E is the ratio of impact energy to specimen thickness equal to 6.672 J/mm (specified by ASTM standard) and h is the sample thickness.

$$E_{delam} = C_E h \tag{2.1}$$

Six industry samples (N1-N6) and one home-made (HM1) sample were impacted at the energy calculated using Eq. (1). Six home-made samples (HM2-HM7) were impacted at energies above and below the calculated E_{DT}, as will be explained in the following section. The latter samples (HM2-HM7) were impacted by calculating the drop height required to produce

<center>(a)</center> <center>(b)</center>
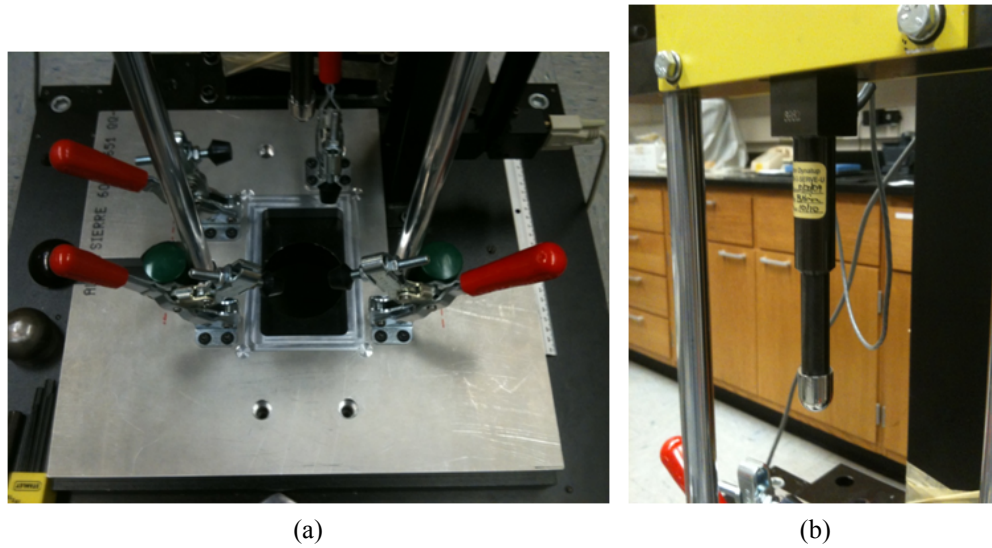
Figure 2.1: Drop-tower configuration for impacting 76.2 mm x 127 mm samples: (a) Base plate and restraints (b) Impactor "tup"

the desired incident energy and adjusting the impactor carriage height accordingly. The total number of impacted samples and the chosen impact energies are shown in Table 2.1.

2.3.2 Data Analysis and Prediction of Delamination Threshold Energy

Force readings are collected from the load cell and acceleration is calculated using Newton's 2nd Law. Velocity v and displacement δ are calculated as functions of time t using the following

Table 2.1: Samples impacted and impact energies

Sample	Chosen Impact Energy (J)
N1-N6	24.2
HM1	28.2
HM2	6.7
HM3	5.7
HM4	4.7
HM5	20
HM6	15
HM7	10

equations:

$$v(t) = v_0 + gt + \int_0^\tau \frac{F(t)}{m} \, dt \tag{2.2}$$

$$\delta(t) = \delta_0 + v_0 t + \frac{1}{2} gt^2 + \int_0^\tau \left[\int_0^\tau \frac{F(t)}{m} dt \right] dt \tag{2.3}$$

where δ_0 is the initial displacement, v_0 is the initial velocity, g is the acceleration due to gravity, F is the force at time t, τ is the contact time, and m is the overall mass of the impactor. The contact time τ is taken to be the time at which load returns to zero from maximum (i.e. $F(\tau) = 0$) and $t = 0$ is taken to be the time of initial contact between the sample and the impactor.

Energy absorbed at time t is calculated from conservation of energy as follows:

$$E_a(t) = \frac{m[v_0^2 - v(t)^2]}{2} + mg\delta(t) \tag{2.4}$$

The load vs. time plot for sample HM1 impacted at approximately 28.2 J is shown in Figure 2.2. Point "A" indicates the local maximum, or the "load drop", which corresponds to the lowest load at which delamination will initiate within the sample, or F_{DT}. The energy absorbed at the time of the first load drop, $E_a(t_{DT})$, is taken to be the delamination threshold energy, or E_{DT}. E_{DT} for sample HM1 was found to be approximately 5.7 J from the first load drop. Using this E_{DT} as reference, samples HM5-HM7 and HM2 were impacted at energies greater than this threshold energy. Samples HM3 and HM4 were impacted at approximately 5.7 J and 4.7 J (at and below the measured E_{DT}), respectively.

The measurements for F_{max} (maximum impact load), F_{DT}, δ_{max} (maximum impact displacement), δ_{DT} (displacement at F_{DT}), and E_{DT} for the "HM" set of samples are shown in Table 2.2. F_{max} increases as impact energy increases, yet F_{DT} only varies approximately 4.56% over the range of impact energies. δ_{max} and δ_{DT} display a similar trend, wherein δ_{max} increases as impact energy increases, but δ_{DT} only varies approximately 2.43% over the range of impact energies. The variation in E_{DT} for the five impacts at separate energies from 6.7-28.2 J is 5.44%.
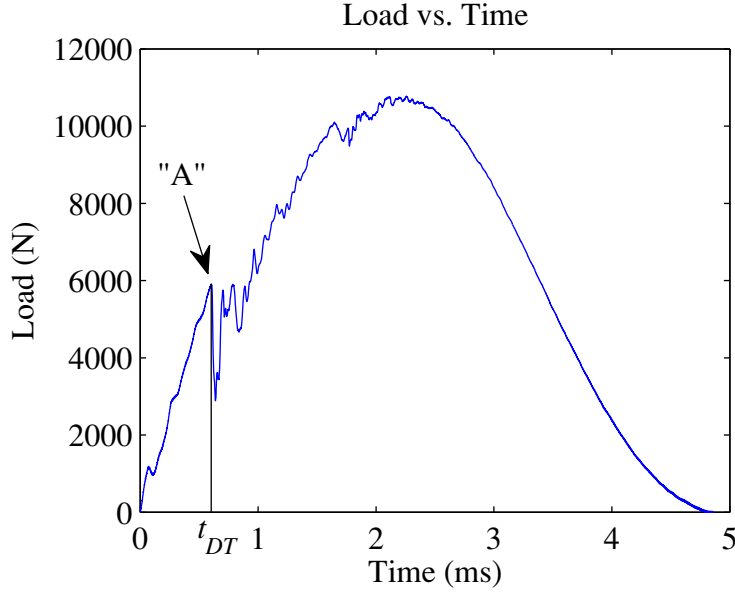
Figure 2.2: Time-history of impact load for sample HM1 impacted at 28.2 J, where "A" is the location of the first drop in load

Table 2.3 shows the same impact measurements for the N set of samples. The samples are impacted at a static incident energy of approximately 24.2 J, and so the drop height to produce this incident energy is only measured once for the entire series of impacts. Therefore, the variation between actual impact energy and nominal impact energy is minimal compared to the HM set of samples. Furthermore, the variations for F_{DT}, δ_{DT}, and E_{DT} over the series of impacts for the "N" samples are 2.97%, 2.62%, and 5.10% respectively. The variation in E_{DT} for the "N" samples is similar to the variation in E_{DT} for the HM samples. The variation in

Table 2.2: Force, displacement, and threshold energy measurements for HM samples impacted from approximately 6.7-28.2 J

Sample	Actual Impact Energy (J)	F_{max} (N)	F_{DT} (N)	δ_{max} (mm)	δ_{DT} (mm)	E_{DT} (J)
HM2	7.13	5583	5583	2.33	1.94	5.53
HM7	9.88	5930	5930	2.78	1.95	5.90
HM6	13.89	7353	6303	3.28	1.94	6.21
HM5	19.46	8973	5743	4.02	1.85	5.44
HM1	28.30	10779	5911	4.87	1.87	5.65

actual impact energy for the "N" samples is approximately 0.35%, and therefore the variation in E_{DT} is not directly related to variation in actual impact energy (and initial velocity). The variation in E_{DT} may be related to the local properties of the sample itself.

Table 2.3: Force, displacement, and threshold energy measurements for N samples impacted at approximately 24.2 J

Sample	Actual Impact Energy (J)	F_{max} (N)	F_{DT} (N)	δ_{max} (mm)	δ_{DT} (mm)	E_{DT} (J)
N1	24.36	7919	7455	5.70	4.64	17.24
N2	24.23	7680	7624	5.63	4.60	17.22
N3	24.25	7780	7366	5.60	4.47	16.29
N4	24.26	7697	7235	5.64	4.41	15.79
N5	24.24	7704	7163	5.65	4.40	15.63
N6	24.10	7929	7732	5.60	4.66	17.66

2.4   Compression After Impact (CAI)

2.4.1   Sample and Fixture Specifications

A standardized method was used to characterize the strength and stiffness properties of the impacted samples. The CAI fixture is shown in Figure 2.3a and consists of top and bottom halves, both of which contain slideplates that constrain the sample on all four edges. The side slideplates have knife-edges, whereas the top and bottom slide plates have flat edges. There is some localized rotational restraint at the top and bottom edges of the sample due to the geometry of the slideplates, although the sample is not considered clamped at these locations since the slideplates are fastened by hand. A constant displacement rate of approximately 0.5 mm/min. was chosen. The ramp cycle begins once the sample is pre-loaded to about 156 N. For the experiment to be successful, the sample must be placed under pure compression, and so the force-displacement curve is monitored to find indication of sample bending or buckling in the form of nonlinearity.

<div style="text-align:center;">(a)   (b)</div>
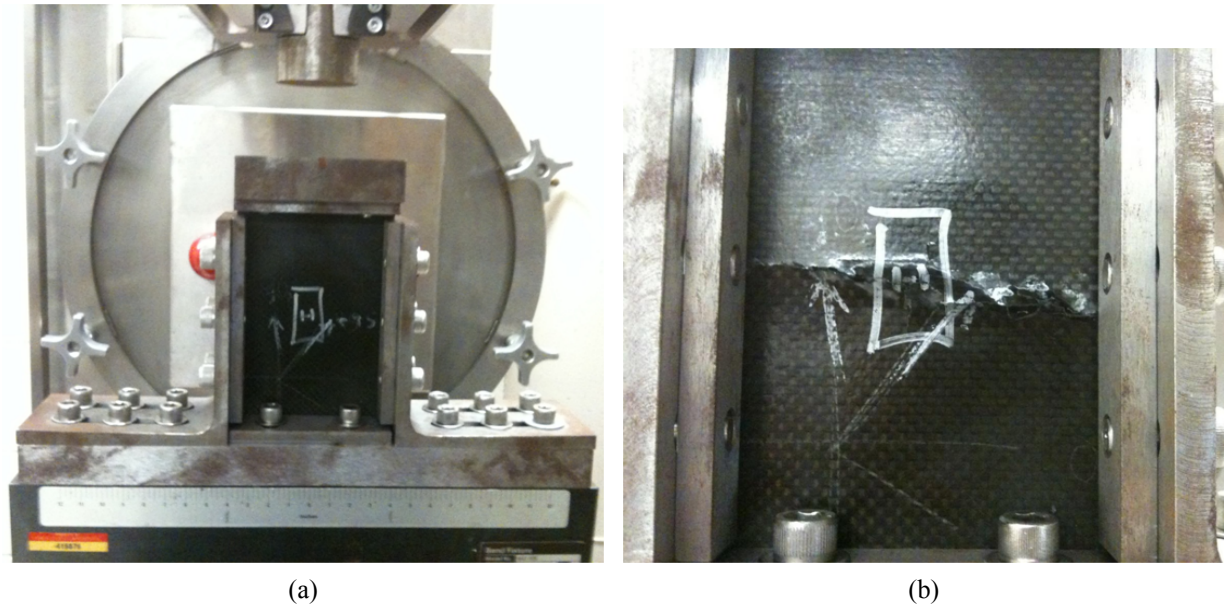
Figure 2.3: Compression after impact configuration (N1 sample shown): (a) CAI fixture (b) Sample failure

Two samples, N1 and HM1, were compressed to failure. Failure is characterized by a rapid lateral crack propagation originating from the impact-damaged region, as shown by the N1 sample in Figure 2.3b. Eight samples (N2-N6 and HM2-HM4) were compressed to a strain value below failure approximately equal to 5000 $\mu\epsilon$ before stopping the test.

2.4.2   Results

Both N1 and HM1 experienced brittle failure and both samples had similar compressive moduli, as seen from Figure 2.4. The compressive moduli and CAI strengths are shown in Table 2.4. Although the compressive moduli for the two sample sets are similar, HM1 has a lower CAI strength than the "industry" quality N1 sample.

Table 2.4: CAI strength and compressive modulus for samples N1 and HM1

Sample	CAI Strength (MPa)	Effective Compressive Modulus (GPa)
N1	234.1	22.19
HM1	184.3	23.26
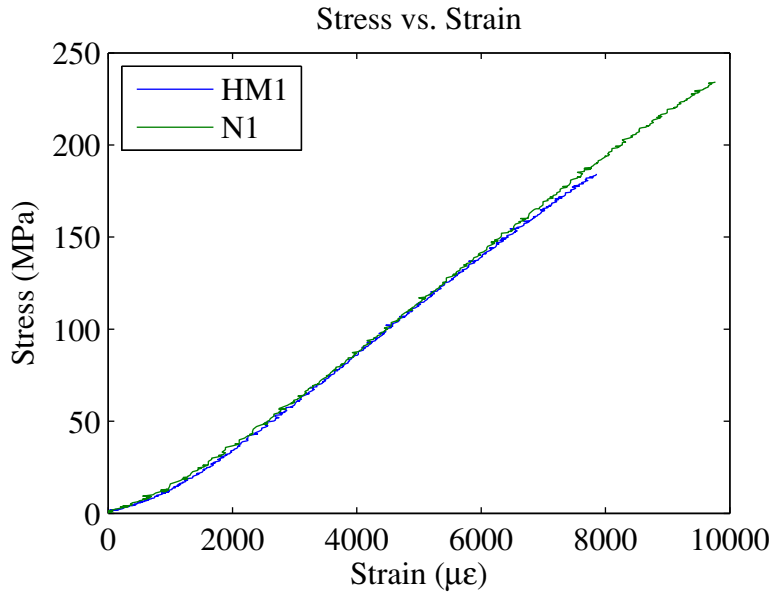
Figure 2.4: Stress vs. strain curve for samples N1 and HM1

The "home-made" samples that were compressed to 5000 με had an average effective compressive modulus of 24.37 GPa with a 2.15% variation in magnitudes over three samples that were tested. Recalling that these samples (HM2-HM4) were impacted at lower energies than sample HM1 (see Table 2.1), it is seen that samples impacted at higher energies may have lower compressive moduli after impact. The "N" set of samples that were compressed to 5000 με (N2-N6) had an average compressive modulus of 23.57 GPa with a 2.13% variation in magnitudes for the five samples that were tested.

2.5 Air-Coupled Through-Transmission Ultrasound (TTU) C-Scans

2.5.1 Scan Setup and Results

Air-coupled TTU scans are collected for all the samples tested using CAI. Two spherically-focused 400 kHz probes are used for the scans. The samples are placed in an array of foam cutouts to prevent the edge effect from sound scattering around the outer edges of the samples.

The scans for the "N" and "HM" sets of samples can be seen in Figures 2.5 and 2.6 respectively. The blue regions towards the center of the samples are regions of low amplitude that

correspond to delamination. The HM samples show a different damage morphology compared to the N samples. The N1-N6 and HM1 samples were impacted at the energy calculated using Eq. 2.1, yet HM1 shows a much larger damage region compared to the "N" set of samples. Furthermore, 2.5 shows an elliptical projected delamination area that is oriented in the -45 fiber direction for all the impacted samples. This directionality is not present in the "HM" set of samples, as seen from the impacts for samples HM1 and HM2 in Figure 2.6. Recalling that HM3 was impacted at E_{DT} and HM4 was impacted 1 J below E_{DT} (see Table 2.1), it is also seen that there are no visible delaminations in both samples. The HM2 sample that was impacted at approximately 6.7 J shows a small delamination area equal to about 20 mm in diameter. Note that the pink artifacts at the corners of some of the samples in Figures 2.5 and 2.6 are due to edge effect at those locations.
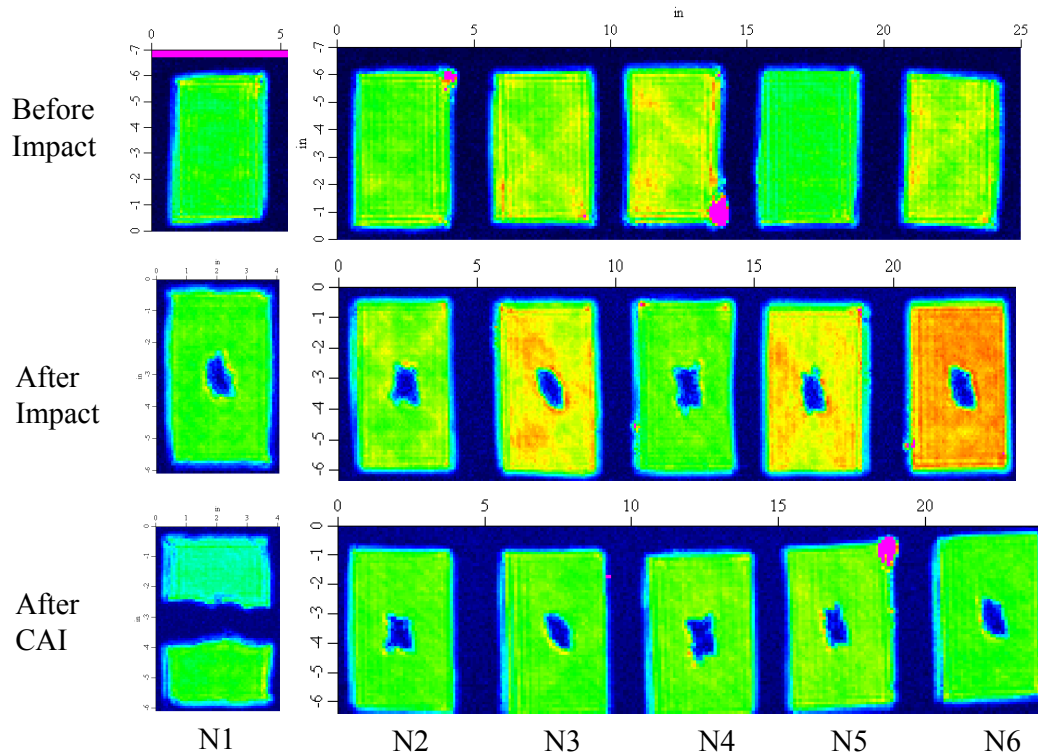
Figure 2.5: Air-coupled TTU scans of the "N" set of samples that were tested using CAI
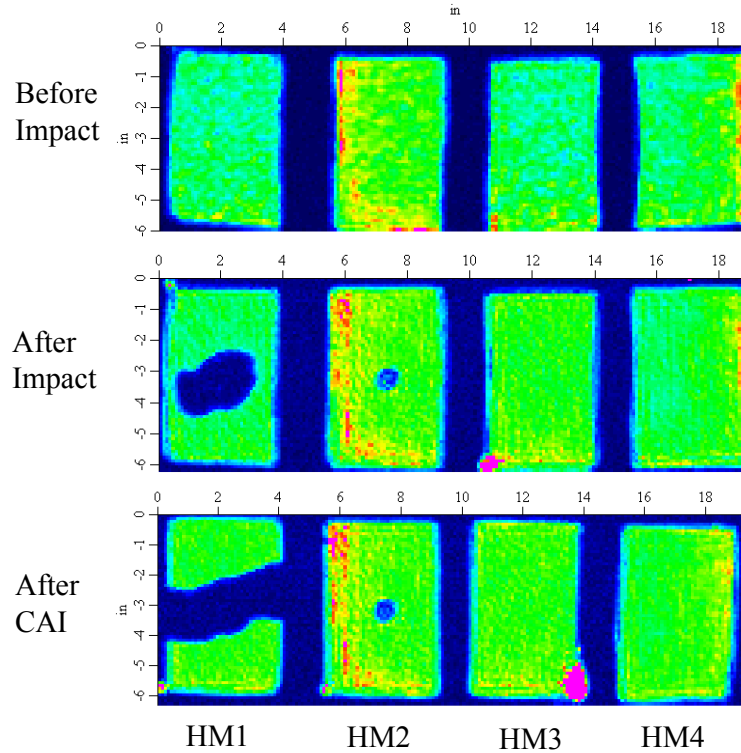
Figure 2.6: Air-coupled TTU scans of the "HM" set of samples that were tested using CAI

The delaminated areas in both sets of samples were measured after impact and after CAI by counting the pixels and calculating area using the pixel resolution. It was found that the damage area increased after CAI but only by about 0.5%. This change is small enough to be on the order of the precision of the scan itself, therefore the damage areas have effectively stayed the same size after CAI to finite strain.

2.6   Conclusions and Future Work

The C-scans for the HM samples show that the predicted E_{DT} is reasonably accurate, considering that HM2 contains delamination and HM4 does not contain any delamination. The characteristic drop in load can be identified in an impacted sample as long as the impact energy is greater than E_{DT}. While t_{DT} changes for different incident energies, δ_{DT} was shown to stay almost constant over different incident energies. The same experiments may be con-

ducted using quasi-static indentation to investigate the dependence of F_{DT} on impact velocity. Moreover, the impacts may be repeated using different mass and constant velocity for different impact energies.

Future experiments would benefit from the reduction in measurement error such that there is lower deviation in the actual incident energy. Furthermore, a repeatable method of scanning the sample using air-coupled TTU would reduce the amplitude variation between separate scans and therefore provide more accuracy for measuring delamination growth due to CAI. Finally, between the two sets of samples that were tested, the "industry"-quality ("N" prefix) samples showed higher CAI strength and similar stiffness compared to the "homemade"-quality ("HM" prefix) samples. The same CAI experiments may be performed using strain gages and acoustic emission methods to investigate damage growth as a function of time during the compression test.

2.7   Acknowledgements

CHAPTER 3.   ULTRASONIC TIME-OF-FLIGHT SHIFT MEASUREMENTS IN CARBON COMPOSITE LAMINATES CONTAINING MATRIX MICROCRACKS

A paper to be submitted to *Review of Progress in Quantitative Nondestructive Evaluation*

A. Subramanian[1], V. Dayal[2], and D. J. Barnard[1]

[1]CNDE, Iowa State University, Ames, IA 50011

[2]Department of Aerospace Engineering, Iowa State University, Ames, IA 50011

3.1   Abstract

Time-of-flight (TOF) shifts are calculated from the fundamental A_0 Lamb mode using air-coupled ultrasound. The technique is applied to a carbon/bismaleimide samples containing varying microcrack density along the length of the sample. The phase and group velocity reduction is inferred from the TOF shift data. Approximate microcrack densities over several segments of the sample are calculated using a simple constant thresholding algorithm and X-ray MicroCT data.

3.2   Introduction

Fiber-reinforced composites have seen widespread application in the military and commercial aviation industries. The need to identify early signs of damage in these composites has greatly increased. Matrix microcracking is one of the initial modes of failure in the laminate,

and is caused due to tensile stresses within the lamina transverse to the ply direction. These microcracks can eventually grow into delamination between adjacent plies [6, 7].

Previous work in the area of microcrack detection in composites have been performed using Lamb wave velocity measurements [13, 14]. The procedure involves capturing the energy of the waves leaking into the coupling medium ("leaky" Lamb waves). Results have shown that the effect of transverse matrix microcracks can be measured through wavespeed changes within the composite laminate.

This paper deals with measuring the effect of microcracking on a composite laminate using time-of-flight (TOF) shift calculations using air-coupled ultrasonic testing (ACUT). The TOF shift measurements are calculated with respect to both group and phase velocities. The fundamental antisymmetric Lamb mode, A_0, is investigated. Ultimately, the bending stiffness loss in the laminate may be inferred from the calculated TOF shifts. We consider the measurement of relative TOF shift using scan data from a transmitter and receiver at fixed separation, as well as TOF shift measured incrementally from scan data with a varying separation between the transmitter and the receiver. Finally, the UT results are correlated with an approximate microcrack distribution along the length of the sample calculated from X-ray MicroCT data.

3.3   Calculation of TOF Shift and Wavespeeds from Measured Data

The TOF shift corresponding to the group velocity can be determined from the cross-correlation between the reference and time-delayed waveforms. This method is employed here due to increased accuracy for attenuated signals compared to the overlap method [15]. The cross-correlation R_{xy} of two discrete time-domain signals $x_n(t)$ and $y_n(t)$ of sample length N and where $n = 0, \ldots, (N-1)$ is given as follows [16]:

$$R_{xy}(k) = \frac{1}{N} \sum_{n=0}^{N-1-k} y_{n+k} x_n, \ k = 0, \ldots, (N-1) \tag{3.1}$$

The cross-correlation can also be rewritten as Eq. 3.2 by using the convolution theorem.

This form can be computed more efficiently using FFTs compared to 3.1.

$$R_{xy}(k) = \mathcal{F}^{-1}\left\{\mathcal{F}\left\{x(t)\right\} \cdot \mathcal{F}\left\{y(t)\right\}^{*}\right\} \tag{3.2}$$

The operators $\mathcal{F}$ and $\mathcal{F}^{-1}$ denote the Fourier transform and inverse Fourier transform respectively, and the asterisk denotes complex conjugate. The time lag corresponding to the maximum of the cross-correlation function between two waveforms is equal to the time delay between the peaks of the waveform, i.e.

$$\Delta T_{g} = \frac{k_{max}}{f_{s}} \tag{3.3}$$

where k_{max} is the lag corresponding to the maximum of the cross-correlation function and f_{s} is the sampling frequency for data collection.

The time delay corresponding to the phase velocity c_{ph} can be found from Eq. 3.4 [1].

$$\Delta T_{ph} = \frac{1}{2\pi f}(\phi_{1} - \phi_{2}) \tag{3.4}$$

ϕ_{1} and ϕ_{2} are the phase spectra of the two waveforms being compared and f is frequency. In order to calculate ΔT_{ph}, we use the phase component at the central frequency. The velocities c_{g} and c_{ph} can be calculated if the wave propagation distance in the sample is known and using ΔT_{g} and ΔT_{ph} calculated using the above methods.

3.4   Ultrasonic Testing

3.4.1   Samples Tested

The samples tested are two 1"x12" IM7/5260 carbon/bismaleimide laminates of [45/0/-45/90]$_{2S}$ stacking sequence that have been thermo-mechanically damaged to induce matrix microcracks. The cured ply thickness of the laminate is approximately 150 μm. Sample B4-1 contains minimal microcracking, whereas sample B4-4 contains a large amount of microcracks in all plies with increasing microcrack density along the length of the sample. The matrix microcracks, or "transverse" cracks, are cracks whose lengths are restricted to the ply or ply-group thickness and whose depths are along the fiber direction.

3.4.2 Immersion UT

Amplitude C-scans are collected in a normal-incidence pulse-echo water-coupled immersion setup using a 10 MHz, 1/4" diameter planar transducer. The schematic of the C-scan is shown in Figure 3.1. The scan results are shown in Figure 3.2. Amplitudes of front-wall echo, first back-wall, and second back-wall echo are observed, where it can be seen that the back-wall echoes in the B4-4 sample attenuate rapidly past the midway point along the length of the sample. This attenuation is presumed to be a result of the increasing microcrack density in the sample.
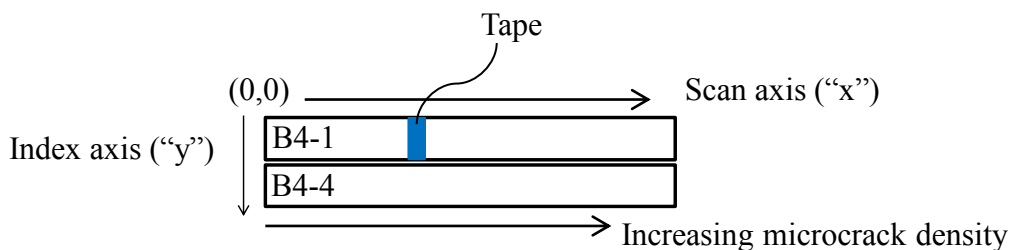
Figure 3.1: Immersion amplitude C-scan schematic (top view)
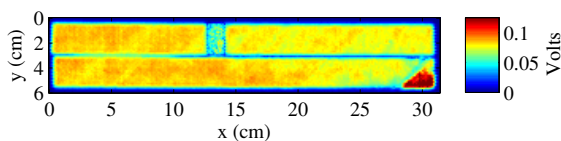
(a) Front-wall echo amplitude
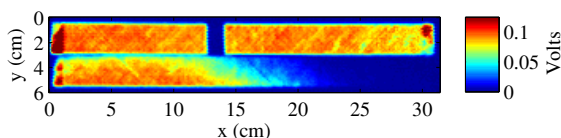
(b) First back-wall echo amplitude
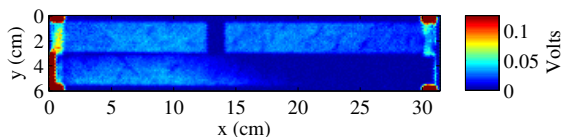
(c) Second back-wall echo amplitude

Figure 3.2: Amplitude C-scans of B4-1 and B4-4 from water-coupled immersion scan

3.4.3 Air-Coupled UT

Two pairs of spherically-focused narrowband transducers at 225 kHz and 400 kHz are used to collect the Lamb wave measurements. The three configurations considered are shown in Figure 3.3. For the configurations shown in Figures 3.3a and 3.3b, the TOF shift was calculated relative to a reference location chosen at the undamaged end of the sample. The configuration in Figure 3.3c permits the calculation of velocity using the increment length of the moving receiver as the change in propagation distance. The TOF shift in this configuration is calculated using a "marching" algorithm. At some location x_i, the ΔT_g and ΔT_{ph} are calculated using the methods outlined in Section 3.3 while using x_{i-1} as a reference. The increment length divided by the respective TOF shift value will yield the local group or phase velocity.

(a) Single-sided TOF shift measurement   (b) Through-transmission TOF shift measurement

(c) Through-transmission velocity measurement
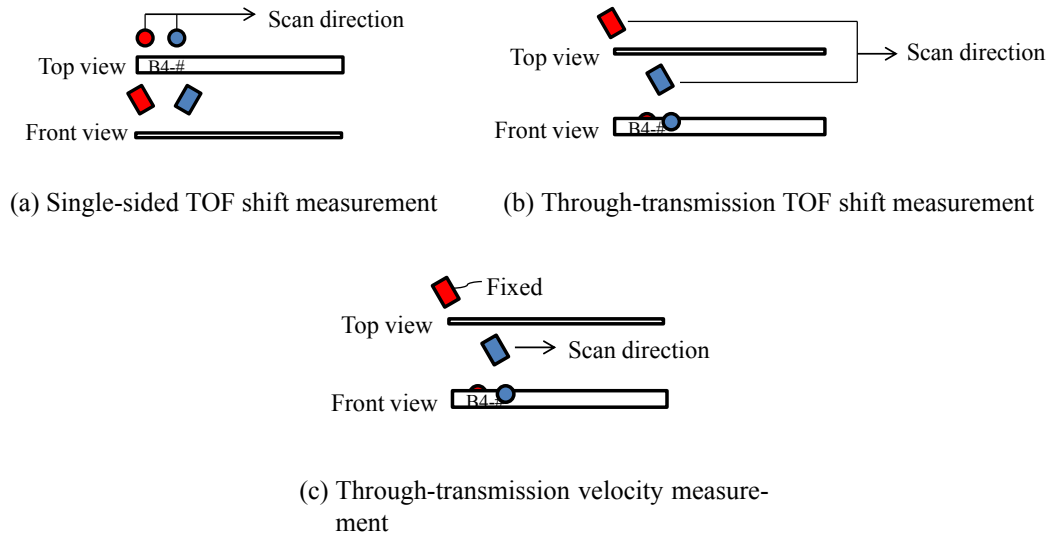
Figure 3.3: Scan schematic for air-coupled scans (transmitter: red, receiver: blue)

The B-scans for the scan configurations in Figure 3.3a and Figure 3.3b are shown in Figure 3.4 for the sample B4-1 using 225 kHz transducers. Figure 3.4a shows a slight curvature over the length of the B4-1 sample for the single-sided setup, where the peaks of the waveform arrive earlier in time. This negative TOF shift results from the shorter air-path due to sample curvature and would not be representative of any phenomenon in the interior of the sample.

The through-transmission setup, 3.3b, mitigates this phenomenon since the air-path between the sample and the transducers remains constant and the effect of sample curvature on TOF shift measurements is greatly reduced. The B-scans for sample B4-4 are shown in Figure 3.5, once again displaying the effect of curvature on the single-sided scan. It is also seen from Figure 3.5b that the waveform peaks arrive at a later time at the end of sample B4-4. This TOF shift is positive, indicating a decrease in A_0 group velocity.

Due to the effect of sample curvature on single-sided scans, the through-transmission setup, 3.3b, is used to calculate TOF shifts in the following section.

(a) Single-sided

(b) Through-transmission
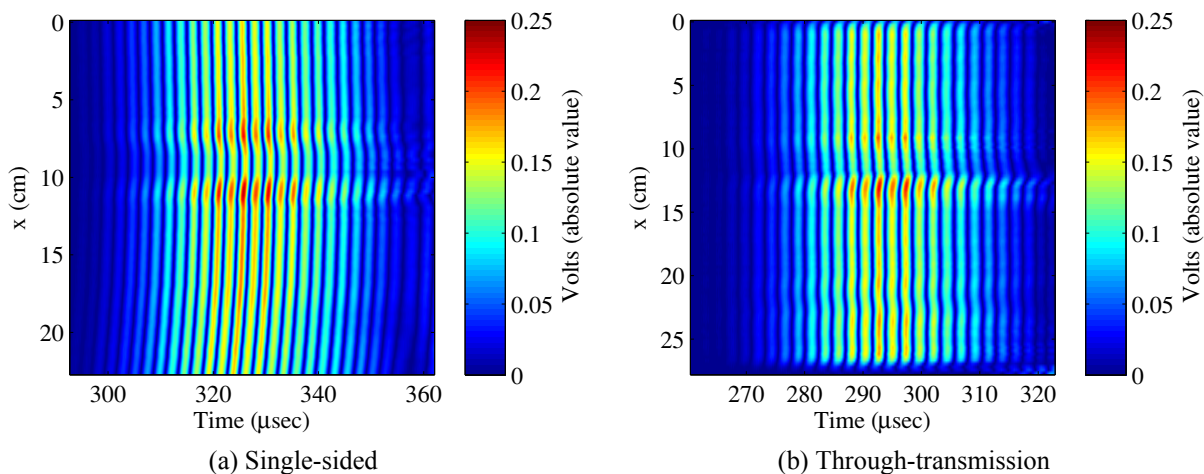
Figure 3.4: B-scans for sample B4-1 scanned using 225 kHz transducers showing the effect of sample curvature on the single-sided setup as compared to the through-transmission setup
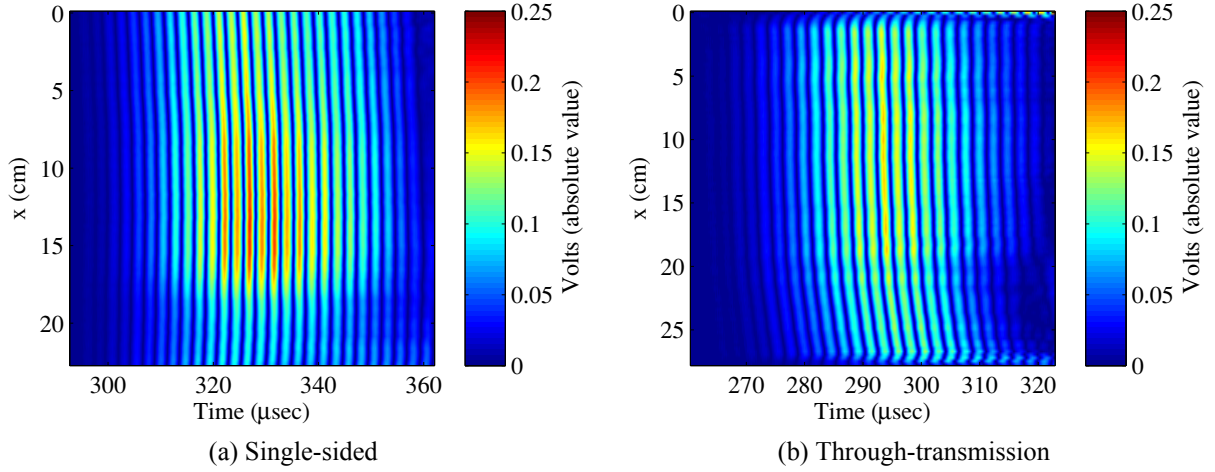
Figure 3.5: B-scans for sample B4-4 scanned using 225 kHz transducers showing the effect of sample curvature on the single-sided setup as compared to the through-transmission setup

3.4.4 TOF Shift and Velocity Calculation Results

The scan configuration shown in Figure 3.3b allows us to calculate the TOF shift with respect to a reference waveform since the transducer separation is constant. If the travel path is known, the velocities can be calculated directly. We consider the TOF shift values by themselves in order to infer the change in wavespeed and laminate stiffness indirectly.

The TOF shifts are shown in Figures 3.6 and 3.7. The reference location for both samples is chosen at x $=1.27$ cm, where there is minimal to no microcracking. Sample B4-4 shows a ΔT_g and ΔT_{ph} increase for both 225 kHz and 400 kHz scans of approximately 3.5 µs. We can infer from this that both the group and phase velocities of the fundamental A_0 mode decrease as microcrack density increases.

The scan configuration shown in Figure 3.3c can be used to calculate the velocity using TOF shifts calculated incrementally. However, in order to capture the waveform in its entirety over the entire sample length, a stationary gate must be used. Figure 3.8 shows the captured A-scan at the reference location (x $= 1.27$ cm) at 225 kHz. We will concern ourselves with the first arriving pulse only.

(a) B4-1   (b) B4-4
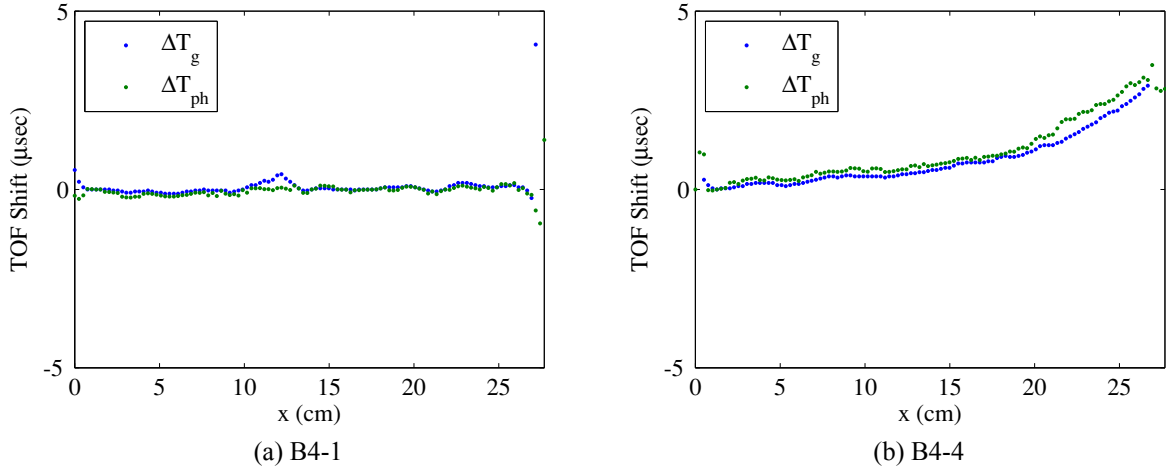
Figure 3.6: TOF shifts along the lengths of samples B4-1 and B4-4 calculated at 225 kHz

The cross-correlation method described in Section 3.3 is used since the phase spectra of the gated waveform is not ideal for the calculation described by Equation 3.4. Since the peak corresponding to the A_0 mode is the dominant feature in the gate, it is assumed that the cross-correlation function R_{xy} will reach a maximum when the dominant peaks of two compared waveforms overlap at some time lag that corresponds to ΔT_g. The constant increment length between x_i and $x_{(i-1)}$, Δx, divided by ΔT_g will yield the group velocity c_g at some location x_i.

The group velocity of the A_0 mode for samples B4-1 and B4-4 are shown in Figure 3.9. Figure 3.9b shows an overall decrease in group velocity of approximately 200 m/s. There is considerable scatter since the peak amplitude decreases rapidly as the receiver is moved along the length of the sample.
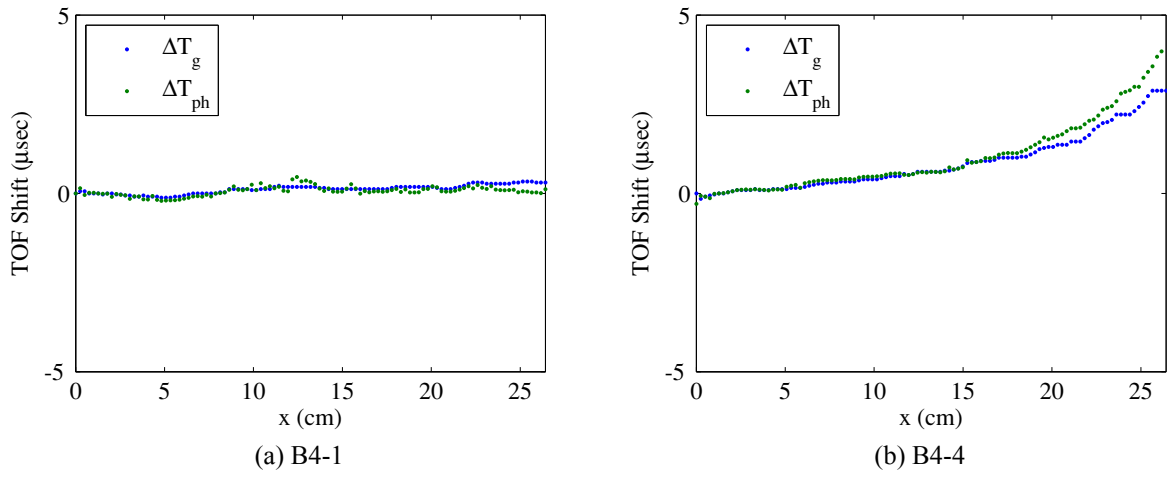
(a) B4-1   (b) B4-4

Figure 3.7: TOF shifts along the lengths of samples B4-1 and B4-4 calculated at 400 kHz
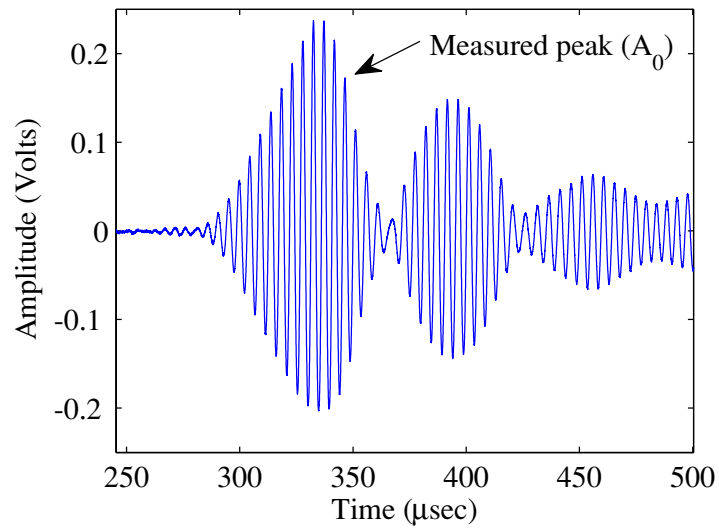
Figure 3.8: A-scan at reference location used for group velocity calculations using 225 kHz transducers
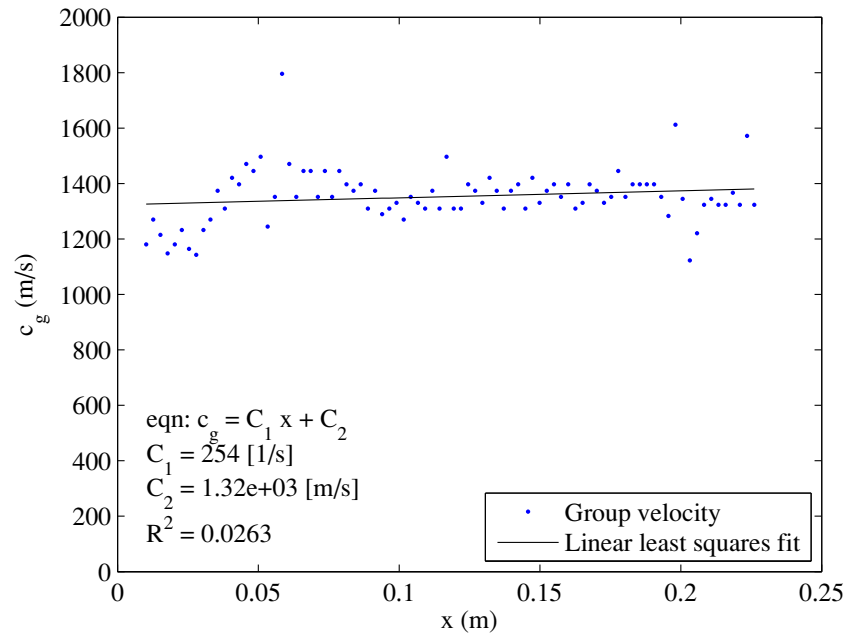
(a) B4-1
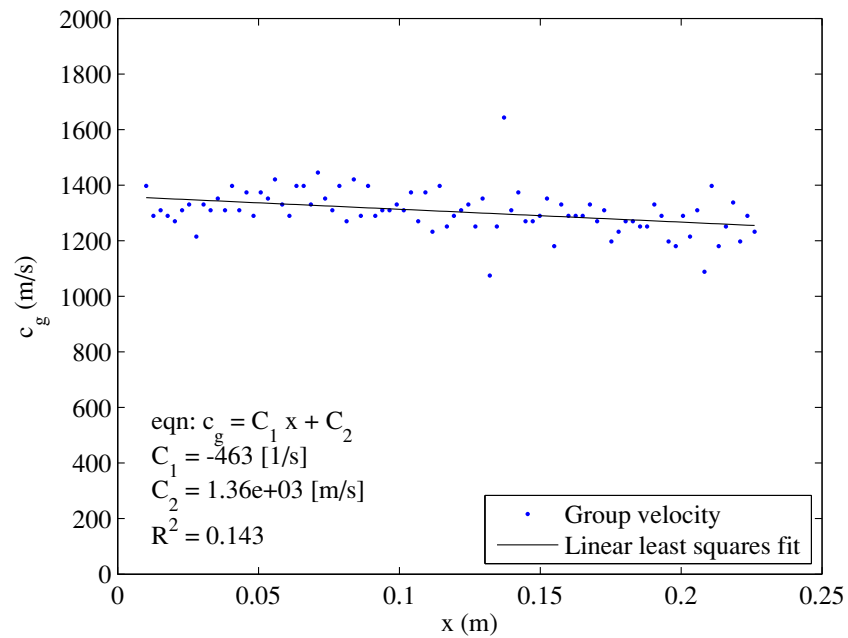
(b) B4-4

Figure 3.9: Group velocity of A_0 mode for samples B4-1 and B4-4

3.5 MicroCT Data

The microcracks have also been detected using X-ray MicroCT. Sample B4-4 was scanned using X-ray microtomography with a resolution of approximately $14\,\mu$m/voxel. A total of seven segments are scanned along the length of the sample as shown in Figure 3.10.
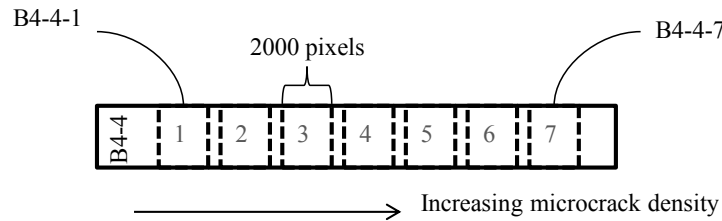
Figure 3.10: Schematic of MicroCT scan

A constant scalar pixel threshold value was used to separate microcrack information from the rest of the sample, and the volume of a portion from a single thresholded segment is shown in Figure 3.11. The threshold value was determined visually such that only the "microcrack" pixels lay above the threshold value. There is some crack information lost due to the fact that the threshold is constant, but it is assumed that the threshold is still high enough to capture the microcrack distribution along the length of the sample. The microcracks can clearly be seen in Figure 3.11 as propagating in the 0°, 90°, and $\pm 45^{o}$ directions. The sample contains a large amount of microcracks within most of the plies through the thickness.

Each segment contains 2000 slices of which approximately 158 slices are removed from the ends of each segment to eliminate scanning artifacts that interfered with the thresholding process. Every 10th slice is processed and the thresholded pixels, or "microcrack" pixels, are counted for the slice. The sample is digitally sliced along the length of the segment, as shown in Figure 3.12.

The results of the pixel-counting are shown in Figures 3.13 and 3.14. It is seen that there is an almost two-fold increase in the amount of "microcrack" pixels from the first segment to the last. The seven segments encompass a region of approximately $17\,$cm along the sample length.
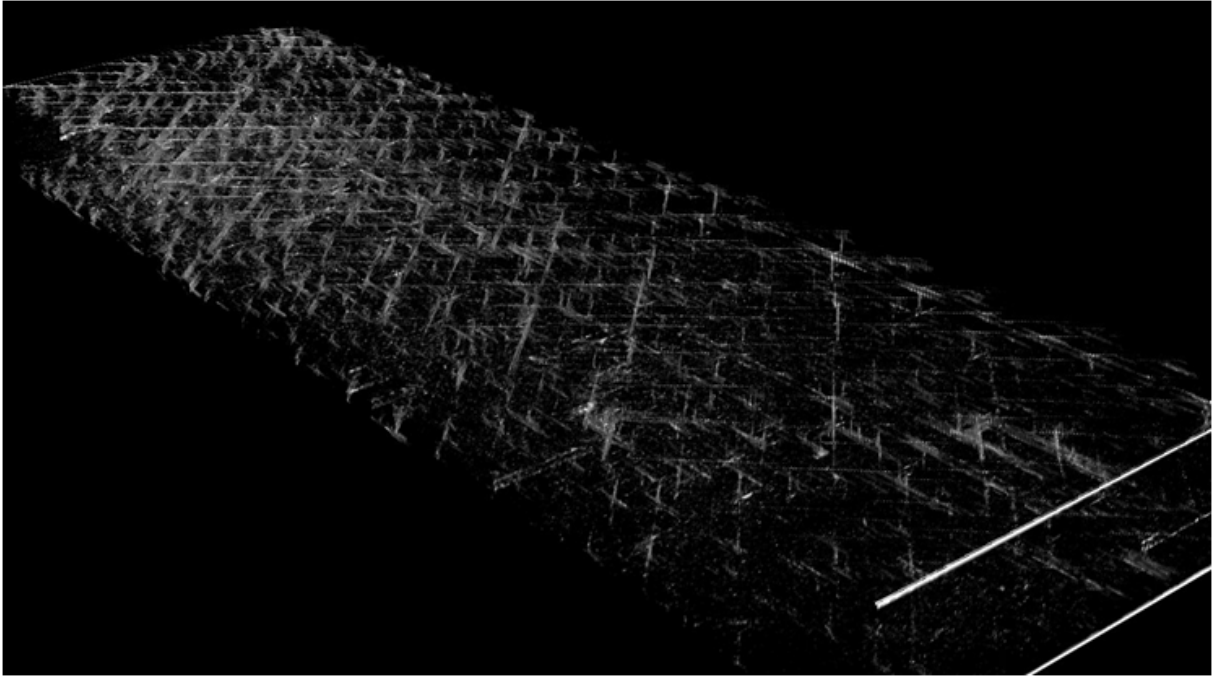
Figure 3.11: Portion of a CT volume from a single segment of the B4-4 sample after thresholding to isolate microcracking

The "jumps" in Figure 3.13 are due to overlap in the discrete scan segments.

Figures 3.6b and 3.13 are shown side-by-side for comparison in Figure 3.15. We see that the increase in measured TOF shift corresponds with the increase in thresholded pixels along the length of sample B4-4. Although the thresholding process does not isolate single cracks or provide information about the crack morphology, it does provide an approximate quantity of the area in the sample occupied by microcracks. Therefore, the effect of increasing microcrack area along the length of sample B4-4 is a reduction in velocity and bending stiffness within the sample.
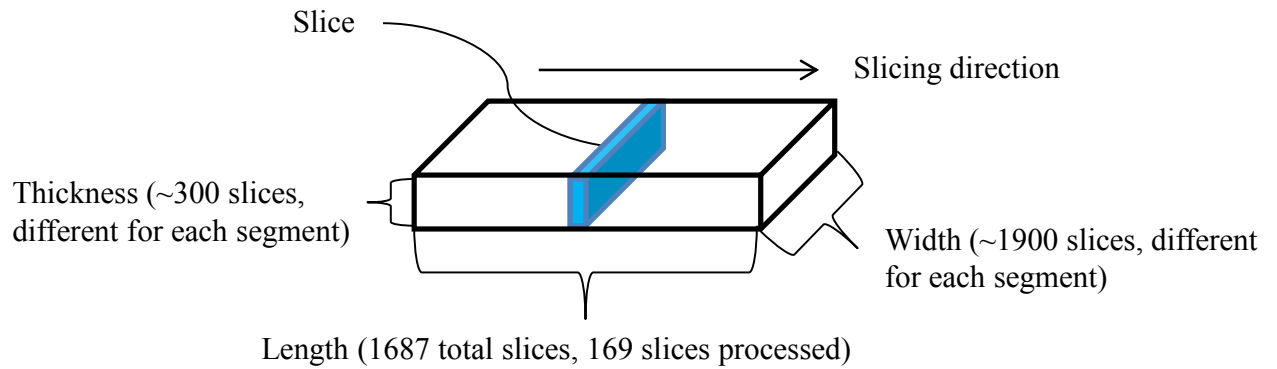
Figure 3.12: Schematic showing a single segment and slicing direction for counting thresh-olded pixels
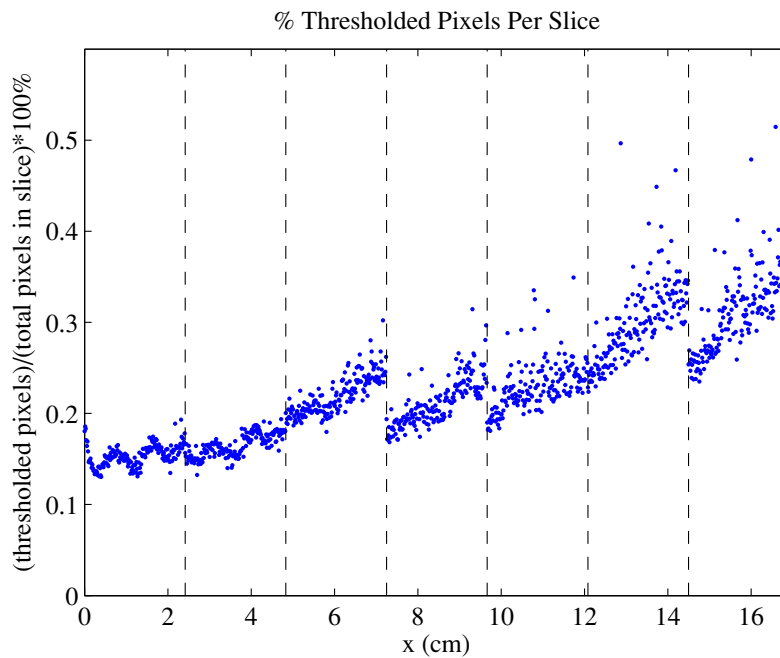
Figure 3.13: Thresholded pixels ("microcrack" pixels) per 10th slice along length of sample B4-4 (NOTE: x = 0 is at the start of the first segment, not sample)
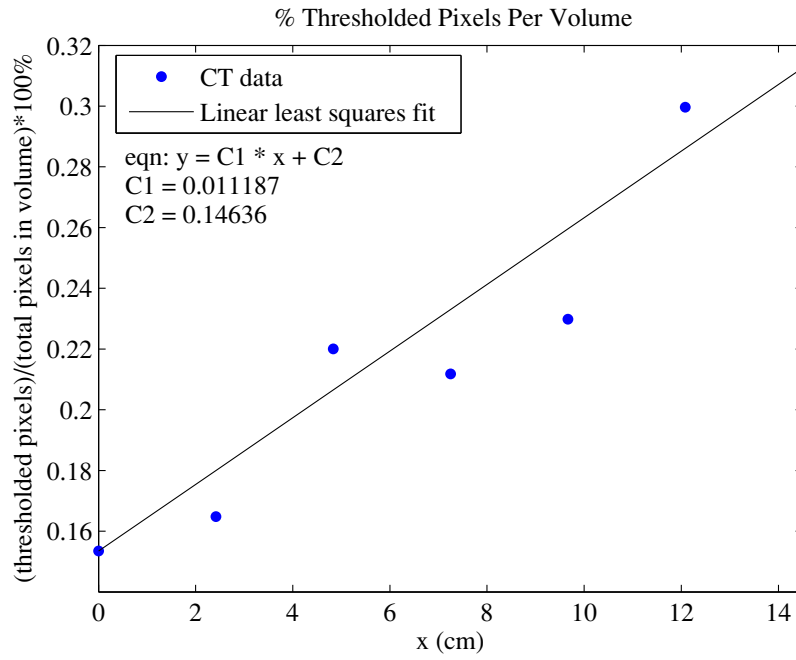
Figure 3.14: Thresholded pixels ("microcrack" pixels) per segment volume for sample B4-4 (NOTE: x = 0 is at the start of the first segment, not sample)
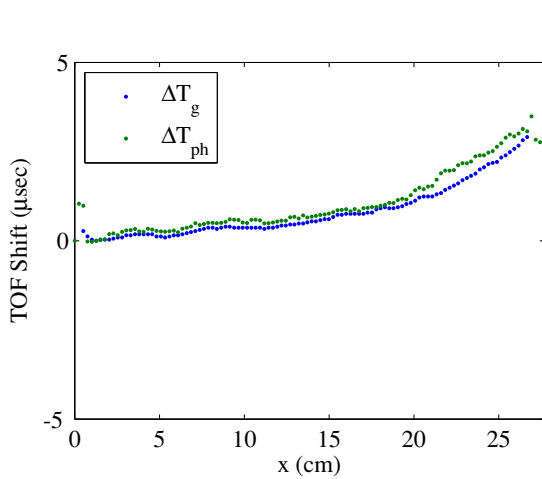
(a) TOF shift measurements at 225 kHz
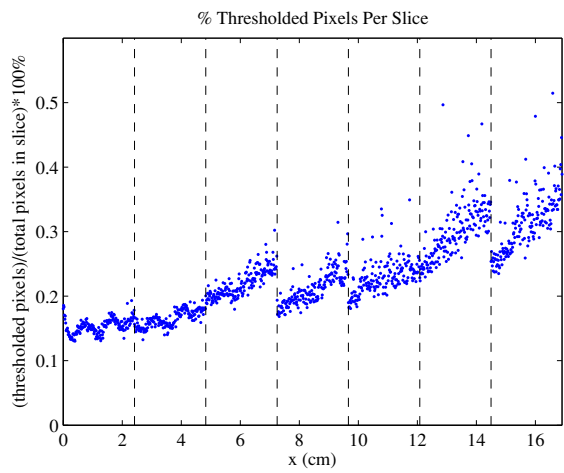
(b) Thresholded "microcrack" pixels per segment

Figure 3.15: Comparison of TOF shift measurements and CT data post-processing for sample B4-4

3.6 Conclusions and Future Work

TOF shift calculations using Lamb wave measurements have been performed. The approach in this paper has shown evidence that the fundamental A_0 mode measured in an air-coupled setup is sensitive to highly microcracked regions within the sample in the form of TOF shifts. In order to accurately measure the TOF shift, systematic error such as signal jitter must be avoided. The cross-correlation method was found to be useful in calculating the time delay between two gated waveforms containing additional reflections in the gate as long as the mode of interest is the dominant feature within the waveform. However, the additional peaks will need to be removed in order to perform phase velocity calculations. The experimentally calculated reduction in phase velocity due to increase in ΔT_{ph} can be corroborated by plotting dispersion curves with reduced stiffness constants.

The MicroCT data, after thresholding to isolate "microcrack" pixels, shows an increase in crack surfaces along the 17 cm region that was scanned. The thresholding process does not yield information about the number of microcracks. A more complex edge-finding algorithm may provide higher accuracy in calculating crack surface area and also in isolating single cracks to calculate microcrack density.

3.7 Acknowledgements

CHAPTER 4.   MATRIX MICROCRACK DETECTION USING ANGLE-BEAM BACKSCATTER MEASUREMENTS

4.1   Introduction

Ultrasonic backscatter techniques are often employed to detect flaws. We consider an angle-beam technique using an ultrasonic transducer at an oblique angle to the sample containing matrix microcracks, as shown in Figure 4.2. The transducer is incident at some angle θ measured from the plate normal at an angle ϕ measured from the 1-axis of the principal material coordinate system (see Figures 4.1 and 4.3). Since the cracks under consideration have depths along the fiber direction, $\phi = 90^o$ describes an incident plane normal to the fiber direction in which the incident wave should reflect from the crack surface. Kinra *et al.* have shown that this angle-beam backscatter technique may be used to image individual microcracks [17, 18]. They investigated thin, quasi-isotropic carbon/bismaleimide laminates and found that an angle of incidence of approximately 25°-30° yields the highest signal-to-noise ratio. In this chapter, we investigate the reflection of a longitudinal wave from a free crack surface to find the highest amplitude reflection coefficient and consider the ply-by-ply refraction of the wave in order to find an optimum angle-of-incidence that maximizes the scattered signal from the crack.
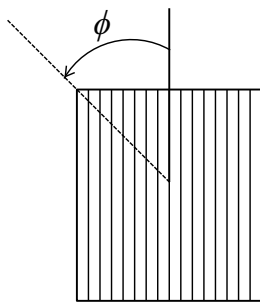
Figure 4.1: Angle of fiber rotation ϕ measured from direction of fiber
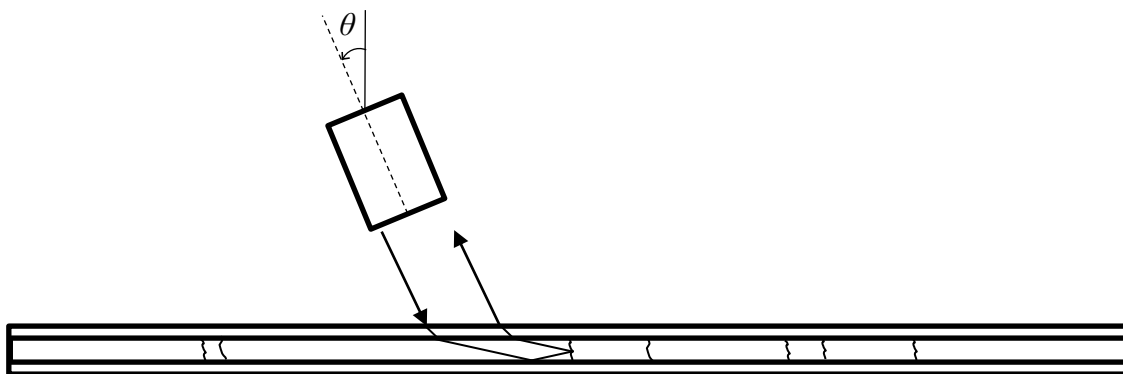
Figure 4.2: Scan schematic for detection of transverse microcracks in a composite laminate where $\phi = 90^{\circ}$ with respect to the middle ply-group containing cracks

4.2 Wave Propagation in a Transversely Isotropic Layer and Minimum Frequency for Inspection

In the case where the dominant wavelength of the ultrasonic pulse is smaller than the layer thickness, we must consider the refraction and reflection of the incident wave at the ply interfaces [19, 20]. It follows that the frequency used for inspection must be on the order of the ply or layer thickness containing the microcrack in order to capture the microcrack backscattering. This is due to the geometry of microcracks, where the length of the crack is typically equal to the layer thickness. In order to find the minimum frequency required to satisfy the above requirement, we must consider the wavespeeds within the media while enforcing the wavelength restriction.

The Christoffel equation for a plane harmonic wave in unbounded media is given by

$$\left[c_{ijlm}n_j n_l - \rho V^2 \delta_{im}\right] p_m = 0 \quad i, j, l, m = 1, 2, 3 \tag{4.1}$$

where c_{ijlm} is the fourth-rank stiffness tensor, n_i is the unit vector in the direction of wave propagation, ρ is density, V is phase velocity, p_i is the particle polarization vector and δ_{ij} is the Kronecker delta. The subscripts denote the 1-2-3 directions in the Cartesian coordinate system with respect to the principle material coordinates as shown in Figure 4.3. In order to obtain a non-trivial solution for p_i, the determinant of the quantity in the square brackets must vanish and three solutions in V^2 are obtained. These solutions correspond to the phase velocities of the three possible wave modes in a generally anisotropic material: the quasi-longitudinal and the two quasi-transverse modes.
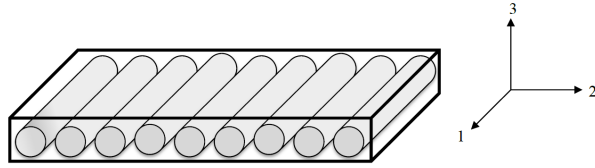
Figure 4.3: Principal material coordinates for a unidirectional ply

A unidirectional ply may be treated as an orthotropic material defined by the following 6×6 stiffness matrix:

$$C_{ij} = \begin{bmatrix} C_{11} & C_{12} & C_{13} & 0 & 0 & 0 \\ C_{12} & C_{22} & C_{23} & 0 & 0 & 0 \\ C_{13} & C_{23} & C_{33} & 0 & 0 & 0 \\ 0 & 0 & 0 & C_{44} & 0 & 0 \\ 0 & 0 & 0 & 0 & C_{55} & 0 \\ 0 & 0 & 0 & 0 & 0 & C_{66} \end{bmatrix} \tag{4.2}$$

The elements C_{ij} are functions of the 9 independent material constants E_1, E_2, E_3, v_{12}, v_{13}, v_{23}, G_{12}, G_{13}, and G_{23} [21]. The fourth-rank stiffness tensor in Eq. 4.1 may be rewritten in

terms of the stiffness matrix by using Voigt notation, where the indices $(11, 22, 33, 23, 13, 12)$ are written as $(1, 2, 3, 4, 5, 6)$. In order to simplify the analysis, we treat the 1-axis as an axis of symmetry, therefore the material is transversely isotropic. In this case, $E_2 = E_3$, $v_{13} = v_{23}$, and $G_{13} = G_{23}$, which yields $C_{66} = C_{55}$, $C_{13} = C_{12}$, and $C_{33} = C_{22}$. We write the characteristic equation arising from the Christoffel equation as

$$\left| \Gamma_{im} - \rho V^2 \delta_{im} \right| = 0 \tag{4.3}$$

where $\Gamma_{im} = c_{ijlm} n_j n_l$ are the Christoffel stiffnesses. Expanding the determinant yields a cubic polynomial in ρV^2 as

$$(\rho V^2)^3 + \alpha (\rho V^2)^2 + \beta (\rho V^2) + \gamma = 0 \tag{4.4}$$

where the coefficients α, β, and γ are given by

$$\begin{aligned}
\alpha &= -(\Gamma_{11} + \Gamma_{22} + \Gamma_{33}) \\
\beta &= -(\Gamma_{12}^2 + \Gamma_{13}^2 + \Gamma_{23}^2 - \Gamma_{11}\Gamma_{22} - \Gamma_{11}\Gamma_{33} - \Gamma_{22}\Gamma_{33}) \\
\gamma &= -(\Gamma_{11}\Gamma_{22}\Gamma_{33} + 2\Gamma_{12}\Gamma_{13}\Gamma_{23} - \Gamma_{11}\Gamma_{23}^2 - \Gamma_{22}\Gamma_{13}^2 - \Gamma_{33}\Gamma_{12}^2)
\end{aligned} \tag{4.5}$$

Figure 4.4 shows the result of solving the characteristic equation for the phase velocity of the longitudinal wave for the case where $\phi = 0^o$ and $\phi = 90^o$ and for the material properties given in Table 4.1. For any ϕ, we must consider the rotated stiffness matrix using the following transformation about the 3-axis [21]:

$$\overline{C} = \begin{bmatrix}
\cos^2 \phi & \sin^2 \phi & 0 & 0 & 0 & \sin 2\phi \\
\sin^2 \phi & \cos^2 \phi & 0 & 0 & 0 & -\sin 2\phi \\
0 & 0 & 1 & 0 & 0 & 0 \\
0 & 0 & 0 & \cos \phi & -\sin \phi & 0 \\
0 & 0 & 0 & \sin \phi & \cos \phi & 0 \\
-\sin \phi \cos \phi & \sin \phi \cos \phi & 0 & 0 & 0 & \cos^2 \phi - \sin^2 \phi
\end{bmatrix} C \tag{4.6}$$

We can see that for the case for $\phi = 90^o$, the longitudinal wave speed is constant since the 1-axis is an axis of symmetry.

Table 4.1: Material properties of a transversely-isotropic IM7/8552 carbon/epoxy lamina ($\rho = 1570 \text{ kg/m}^3$)

E_1 (GPa)	E_2 (GPa)	E_3 (GPa)	G_{12} (GPa)	G_{23} (GPa)	G_{13} (GPa)	ν_{12}	ν_{23}	ν_{13}
161	11.4	11.4	5.17	3.92	5.17	0.32	0.45	0.32
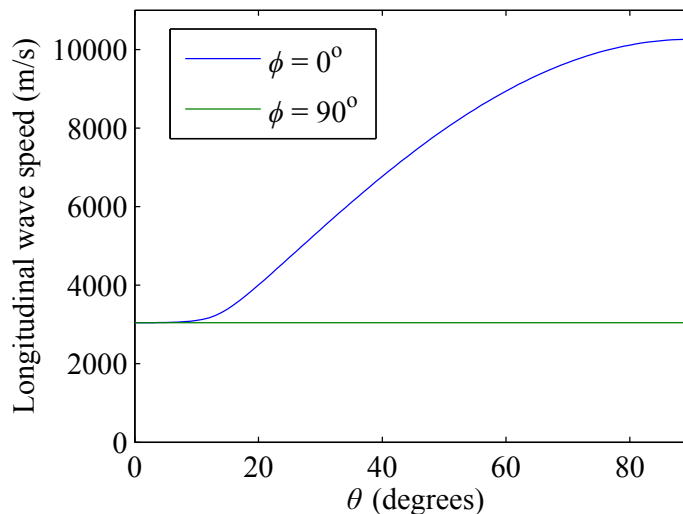
Figure 4.4: Longitudinal wavespeed in a transversely-isotropic layer

The analysis presented here will consider $\phi = 90^\circ$. We see from Figure 4.4 that the longitudinal wavespeed, V_l, is constant for $\theta = 0^\circ$ and for any arbitrary ϕ. We consider the case where $\mathbf{n} = (0, 1, 0)$, where the solution for the longitudinal wave yields

$$V_l = \sqrt{\frac{C_{22}}{\rho}} \tag{4.7}$$

As mentioned earlier, the dominant wavelength λ of the ultrasonic pulse must be less than the layer thickness d. From this requirement, we can write the minimum frequency required f_{min} as

$$f_{min} = \sqrt{\frac{C_{22}}{d^2 \rho}} \tag{4.8}$$

where ρ is the density of the layer.

4.3 Reflection from a Free Surface and Refraction at Ply Interfaces

The reflection from a microcrack within a layer is modeled as a reflection from a stress-free surface. This assumption is valid as long as the particle displacements of the impinging wave are much smaller than the crack opening. Rokhlin *et al.* have developed a generalized Snell's law in order to treat the problem of reflection and refraction at ply interfaces [22]. The coordinate system is defined by the incident plane and the interface plane. Snell's law requires that the projection of all incident, reflected, and refracted waves on the interface plane must be equal. Furthermore, the incident, reflected, and refracted waves all lay within the incident plane.

Three pure modes, one longitudinal and two shear that are polarized in mutually orthogonal directions, exist if the condition $\mathbf{p} \cdot \mathbf{n} = 1$ is satisfied for one of the modes. If the condition $\mathbf{p} \cdot \mathbf{n} = 0$ is satisfied, then only one of the modes is guaranteed to be pure [19]. For the case of the transversely isotropic layer, there are three pure modes generated for $0^{\mathrm{o}} < \theta < 90^{\mathrm{o}}$ when $\phi = 90^{\mathrm{o}}$. The pure longitudinal mode is polarized in the direction of of wave propagation, the fast transverse wave (SH) is polarized normal to the incidence plane, and the slow transverse wave (SV) lies orthogonal to the longitudinal wave in the incident plane. Since the solution for the reflected and refracted waves are bound to the incident plane, the reflection coefficients for the SH wave are zero for any θ when $\phi = 90^{\mathrm{o}}$.

Since the configuration considered (i.e. $\phi = 90^{\mathrm{o}}$) produces a plane of isotropy for any incident angle, we calculate the reflection coefficients using the simplified approach for an isotropic material. For the case of an incident longitudinal wave on a free surface, we write the reflection coefficient R_{LL} for a reflected longitudinal wave V_L as [23]

$$R_{LL} = \frac{\cos^2 2\theta_{SV} - \dfrac{V_{SV}^2}{V_L^2} \sin 2\theta_{SV} \sin 2\theta_L}{\cos^2 2\theta_{SV} + \dfrac{V_{SV}^2}{V_L^2} \sin 2\theta_{SV} \sin 2\theta_L} \tag{4.9}$$

where $\theta_L = \theta$ and θ_{SV} is found from Snell's law as

$$\theta_{SV} = \arcsin \left[\frac{V_{SV}}{V_L^i} \sin \theta \right] \qquad (4.10)$$

where V_L^i is the velocity of the incident longitudinal wave and V_{SV} is the velocity of the reflected shear vertical wave in the incidence plane. For the properties given in Table 4.1, $V_L \approx 3044$ m/s and $V_{SV} \approx 1580$ m/s. The longitudinal-longitudinal reflection coefficients are shown as a function of incident angle in Figure 4.5. In this figure we see that the maximum reflection coefficient is obtained when the incident wave is normal to the 1-3 plane (i.e., $\theta = 90^o$).
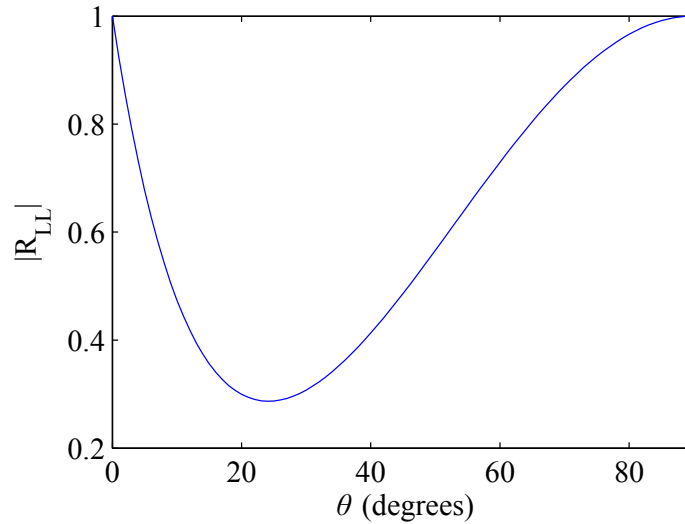
Figure 4.5: Longitudinal-longitudinal reflection coefficient from a free surface in a transversely-isotropic layer where $\phi = 90^o$ vs. angle of incidence

In order to calculate the angles of refraction at a ply interface, we once again use Snell's law. We consider a longitudinal wave incident in water ($V_L^i \approx = 1500$ m/s). Since the continuity of the interfacial component of velocity must be satisfied for Snell's law, we conclude that the angles of refraction, θ_t, remain the same for a given ply direction ϕ. The refraction angle within an interior layer is influenced by the velocity of the initial incident medium (i.e., water) and the layer orientation ϕ. This phenomenon can also be seen from the generalized Snell's law approach, wherein the only inputs to the problem are the incident interfacial component of the

velocity vector and the wave propagation direction [22]. Therefore, the refraction angle θ_t is simply

$$\theta_t = \arcsin\left[\frac{V_L}{V_L^i}\sin\theta\right] \tag{4.11}$$

Figure 4.6 shows the angles of refraction within the transversely isotropic layer at $\phi = 90^\circ$. It is seen that $\theta = 30^\circ$ is a critical angle and the refracted longitudinal wave ceases to propagate past this angle. We can see from the fact that θ_t approaches 90° when θ approaches 30° and from Figure 4.5 that the reflection coefficient is highest just before the critical angle. The implementation of the generalized Snell's law using MATLAB functions is given in the Appendix.
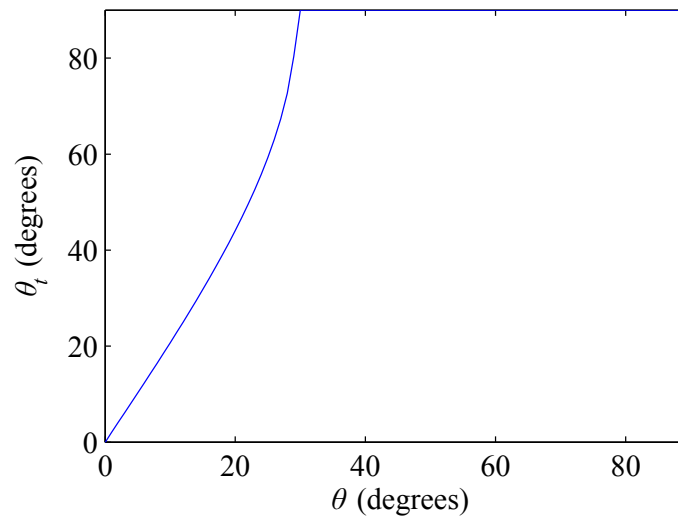
Figure 4.6: Refraction angles in a transversely-isotropic layer for a longitudinal wave incident in water at $\phi = 90^\circ$

4.4   Experimental Results

A 2.54 cm wide $[0_4/90_4]_S$ laminate comprised of unidirectional IM7/8552 carbon/epoxy prepreg was considered for the experiments. Matrix microcracks were introduced in all plies using thermal fatigue. The cracks encompass the entire ply-group length and so the minimum

frequency required can be calculated using Eq. 4.8 where d is equal to the smallest continuous layer, or ply-group, in the laminate. In this case, $d \approx 0.5$ mm if we assume a nominal ply thickness of 125 μm. This yields an f_{min} of approximately 6 MHz.

A 10 MHz, 6.35 mm diameter probe with a 3.175 cm focal length is considered for angle-beam backscatter inspection of the laminate. Microscopy is performed on two edges of the laminate to determine the distribution and number of cracks in the 0° and 90° directions. Since the sample contains two outer ply-groups of 0° plies, the sample was scanned on both sides of the sample (sides "A" and "B") such that the highest reflected amplitude could be obtained from the microcracks. Figure 4.7 shows the amplitude C-scans for the first and second (upper and lower) 0° ply-groups for $\theta \approx 25^o$. The high-amplitude regions shown in red correspond to a peak in the backscatter noise corresponding to reflection from a crack. Figure 4.8 shows the A-scan of a location on the sample where a reflected signal from a microcrack is received by the transducer.

(a) Side "A" (b) Side "B"
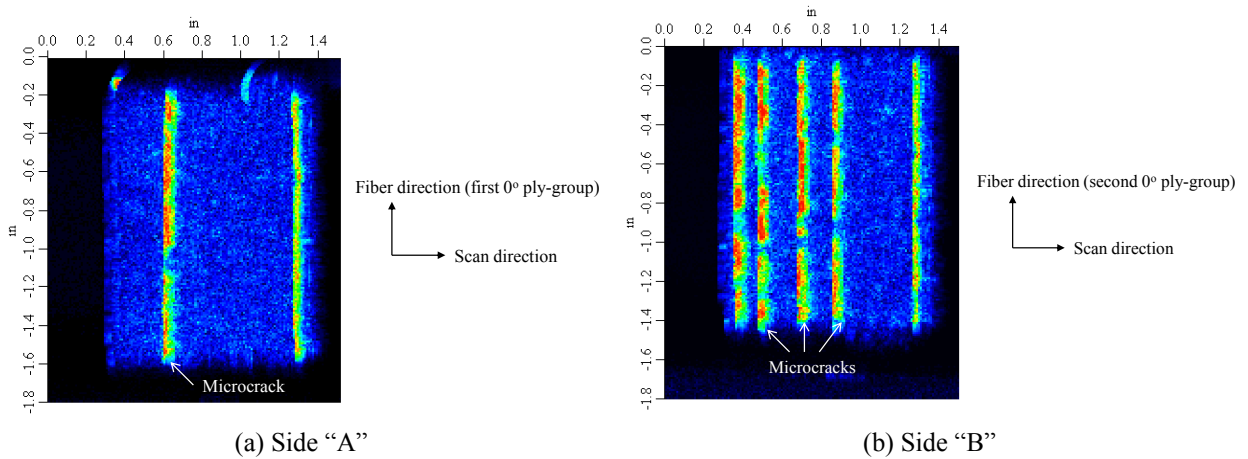
Figure 4.7: Amplitude C-scans for the upper and lower 0° ply-groups for $\theta \approx 25^o$

The data for the sample scanned from side "A" was processed by moving the gate later in time to find reflections from microcracks in the opposite 0° ply group. Figure 4.9 shows the amplitude C-scan for cracks in the deeper ply group. These cracks are barely visible and the crack from the side "A" ply-group is still present in the C-scan. The significant attenuation in
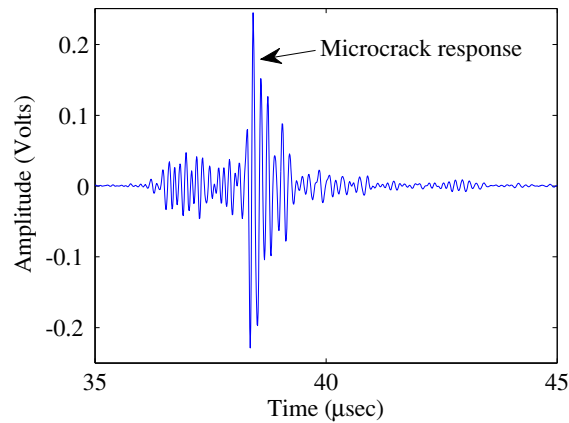
Figure 4.8: A-scan showing a reflected peak from a microcrack within the laminate

the sample (and possibly due to microcracking) reduces the sensitivity to cracks in deeper plies and poses a limitation for this technique in application to thick laminates. It should be noted that this plot is 'as scanned' and no signal processing has been performed.
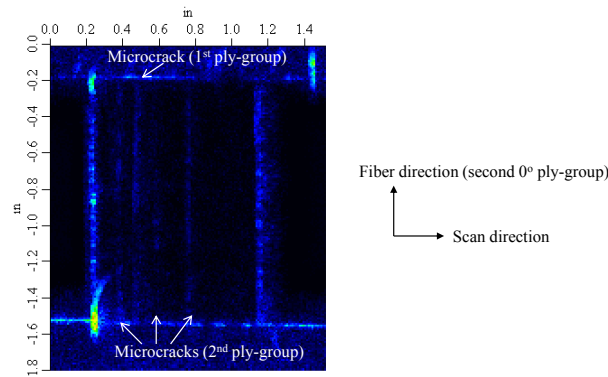
Figure 4.9: Amplitude C-scan showing cracks in the deeper ply-group of 0° plies

The effect of the incident angle θ was tested by inspecting the cracks within the middle ply-group of 90° plies at $\theta \approx 0^o, 15^o, 30^o$ and 45°. The results are shown in Figure 4.10. For $\theta = 0^o$, the high amplitude regions in red correspond to reflections from resin pockets within the laminate. We see that the microcracks (vertical lines in the C-scan) are visible for $\theta \approx 15^o$ and 30°, however they do not appear in the C-scan at $\theta \approx 45^o$. This is consistent with the result in the previous section, that $\theta = 30^o$ is a critical angle, beyond which the refracted waves are

evanescent.

$\theta = 0^o$ $\theta = 15^o$

Fiber direction (90° ply-group)

Scan direction

$\theta = 30^o$ $\theta = 45^o$
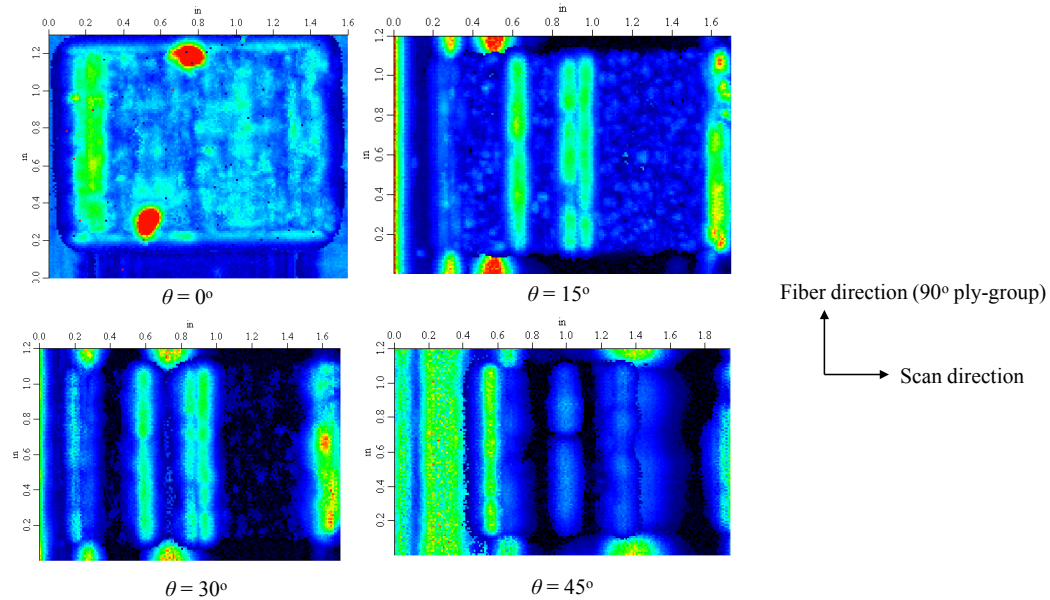
Figure 4.10: Variation of microcrack reflections with incident angle for the middle ply group of 90° plies

4.5   Conclusions and Future Work

The simple analysis is Section 4.3 suggests that for a transversely-isotropic layer with the properties given in Table 4.1, the optimum angle of inspection is approximately 25° to 30°. In order to verify the theoretical results experimentally, the reflection coefficients must be measured accurately for various angles of inspection. The experimental results, as verified by theory, suggest that beyond the critical angle, the peaks in the backscatter signal corresponding to microcrack reflections cease to appear. The minimum frequency required poses a limitation on inspection of thick laminates that do not contain any ply groups (i.e., $d \approx 125\,\mu m$). Although transducers above 25 MHz may be used successfully to detect cracks in single plies, there is still a difficulty in detecting cracks deeper within the laminate due to attenuation of the backscatter signal.

CHAPTER 5.   DETECTION OF MICROCRACKS INDUCED BY LOW-ENERGY IMPACTS

5.1   Introduction

Impact energies below delamination threshold energy described in Chapter 2 produce matrix microcracks in the local impact region. The microcrack density within the laminate may be low if the impact energy is much lower than E_{DT}. The microcracked samples investigated in Chapter 3 have been thermo-mechanically damaged to produce a high density of microcracks throughout the laminate. In this chapter, we consider the inspection of laminates that have been impacted either at or below the delamination threshold energy. It is assumed that the damage mode in the local impact region is primarily microcracking and the microcrack density in this region is low.

An immersion ultrasound pulse-echo mode approach is considered first to observe the attenuation in the first and second back-wall echoes of the impacted region. The methods employed in Chapter 3 are used to calculate the Lamb wave velocities in the sample HM2 and HM3 (impacted at approximately 6.7 J and 5.7 J respectively) from Chapter 2. We recall that sample HM2 had visible delamination and HM3 had no discernable signs of delamination in the normal incidence TTU air-coupled scan results.

5.2 Immersion Ultrasound Scans

A 10 MHz, 6.35 mm diameter planar transducer was used to scan samples HM2 and HM3 in a water-coupled immersion setup. Figure 5.1 shows the second-back wall echo amplitude C-scan of samples HM2 and HM3. It is evident that the large, circular low-amplitude region at the center of sample HM2 is due to delamination. Figure 5.2 shows the magnified amplitude C-scan images for sample HM3, where the color palette has been adjusted based on the maximum and minimum amplitudes for each echo. The impact location is at the bottom right corner of the scan area and there is a low amplitude feature at the bottom right of the C-scans for both the first and second back-walls. This low amplitude region is slightly larger in the second back-wall C-scan, perhaps owing to the repeated reflection within the damage region. Furthermore, the first back-wall C-scan contains low amplitude regions away from the impact region which are not present in the second back-wall C-scans. This phenomenon could possibly be due to the surface roughness of the sample, the effects of which are averaged over repeated internal reflections in the sample.
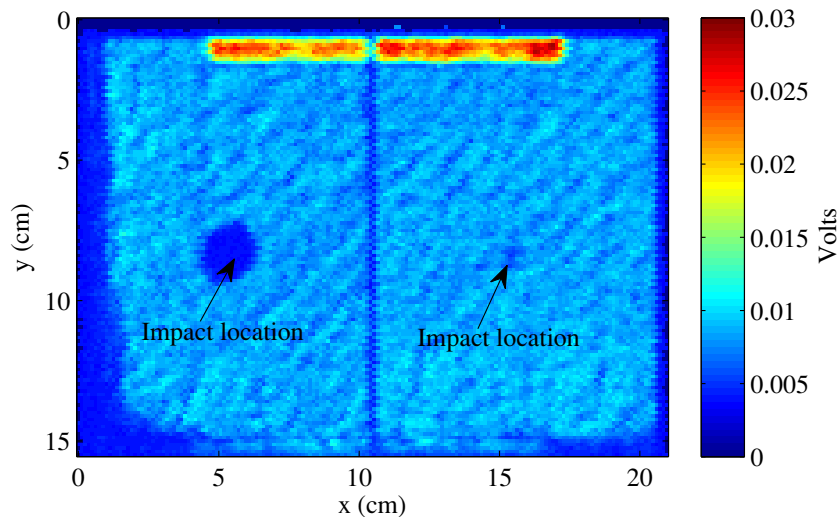
Figure 5.1: Second back-wall echo amplitude C-scan of samples A2 (left) and A3 (right)

(a) First back-wall echo   (b) Second back-wall echo
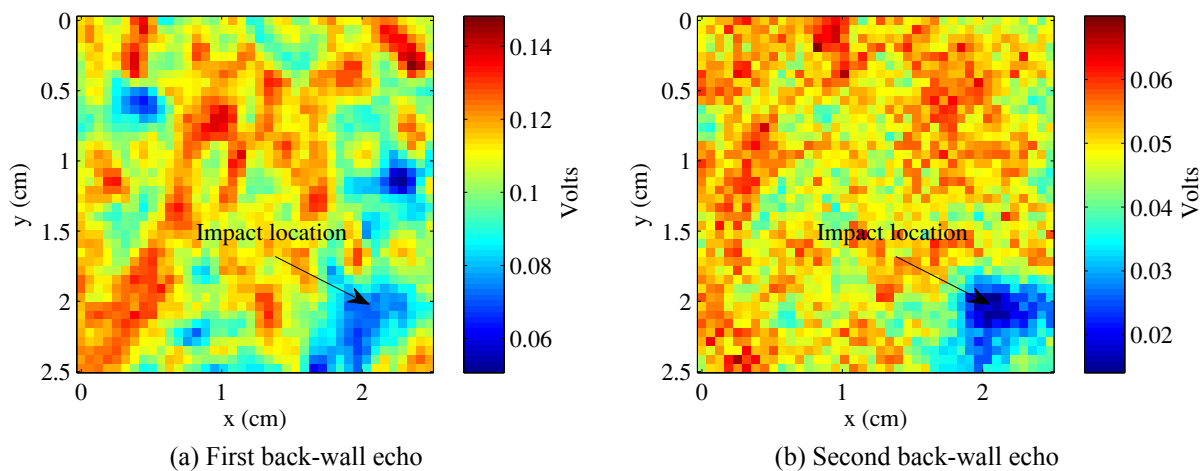
Figure 5.2: Amplitude C-scans of sample HM3 impacted at the delamination threshold energy

5.3   Lamb Wave Velocity C-scans

The velocity measurement setup considered in Section 3.4.3 is used here in a single-sided configuration to calculate the group velocities of the A_0 mode. Once again, a pair of focused 225 kHz air-coupled transducers are used for the scans. The phase velocity dispersion curve for the laminate considered is shown in Figure 5.3

We assume that the group velocities are approximately the same as the phase velocities in magnitude, as seen from the measurements made using the same frequency in Chapter 3. The inspected sample is approximately 4.3 mm thick, and so the frequency-thickness product is approximately unity. From Figure 5.3, we see that only the two fundamental modes, S_0 and A_0, are generated in the laminate.

The velocity "C-scans" are performed using the same "marching" algorithm described in Section 3.4.3 while indexing in the perpendicular y-direction. Figure 5.4 displays the results of the scans. Sample HM3 does not show any visible changes in group velocity, however we see that the magnitude of the group velocity is approximately 1500 m/s. This value agrees well with the wavespeed for the A_0 mode shown in Figure 5.3. Sample HM2, however, shows a
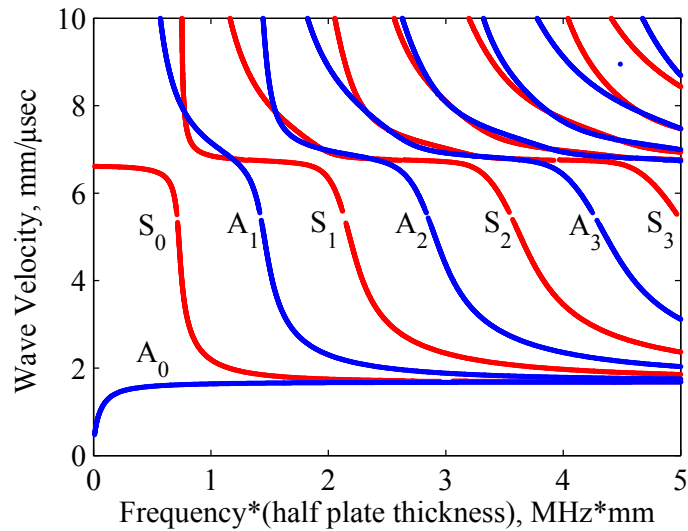
Figure 5.3: Phase velocity dispersion curves for a $[+45/0/-45/90]_{4S}$ laminate made from unidirectional IM7/8552 carbon/epoxy prepreg (NOTE: the anti-symmetric modes are shown in blue and the symmetric modes are shown in red)

circular region of faster group velocity corresponding to the delamination induced by impact.

There are no known analytical solutions for the case of scattering of Lamb waves incident on a delamination. However, numerical solutions and FEM have been done in this area [24, 25]. The results of this previous work have shown evidence that the incident A_0 mode converts into several wave groups upon interacting with the delamination and the wavespeed measurement employed in Chapter 3 would not guarantee a measurement of the group velocity of any one mode out of the several that are generated. It is however possible that over the delaminated region one of the converted modes from the incident A_0 may be measured whose velocity is greater.

(a) HM3   (b) HM2
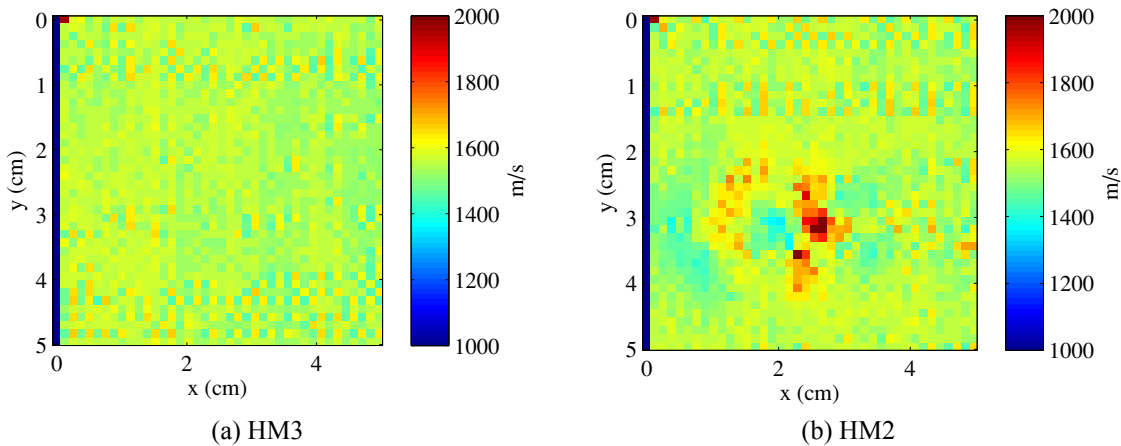
Figure 5.4: Velocity "C-scans" for samples HM3 and HM2 approximately centered over the impact regions

5.4 Conclusions and Future Work

The detection of microcracks induced by low-energy impacts on composite laminates is of great importance due to the localized nature of the damage and the complex damage morphology arising from mixed-mode loading. Although immersion UT provides meaningful results, ultimately a field-deployable inspection method would be ideal. Air-coupled scanning, especially with respect to Lamb waves, shows potential for detection of local stiffness loss due to microcracking induced by impact damage, although the A_0 mode is not seen to change appreciably for lower microcrack densities. Since microcracking reduces the in-plane stiffness in the laminate, the symmetric modes should also be investigated. However, the difficulty posed by receiving symmetric modes in air-coupled configurations is due to the low amount of energy that "leaks" into air (due to the difference in acoustic impedances between air and solid). These modes, however, can be observed more easily in using a fluid couplant and their response to in-plane stiffness loss due to microcracking may be measured using immersion UT.

CHAPTER 6.   CONCLUSION

Damage detection in fiber-reinforced composites has been investigated using a variety of ultrasonic techniques. The damage modes during a mixed-mode impact loading event were identified using an energy threshold. High microcrack densities were found to be detectable under conventional scanning modes, including immersion UT. The fundamental antiysymmetric Lamb mode A_0 was found to be sensitive to changes in laminate stiffness caused by varying microcrack density. The application of the TOF shift and velocity measurement techniques to lower microcrack densities must be investigated more thoroughly, as the presence of microcracks anywhere within a laminate and in arbitrary morphologies may serve as initiation points for macroscopic failure in the laminate. The pixel-thresholding algorithm applied to the X-ray MicroCT data is a simple yet useful way to gauge the relative microcrack density in a region.

Angle-beam backscatter measurements are ideal for thin laminates with ply groups since microcracks propagate continuously through adjacent plies of the same orientation. However, this is not the case for many practical applications, and the technique must only be considered for the subset of laminates for which damage in deeper plies (i.e., farther away from the transducer) is not of concern. For single-ply inspections, the frequency must be on the order of 20-25 MHz. This puts a large restriction in the amount of plies that can be investigated due to frequency-dependent attenuation within the sample.

There is evidence to show that stiffness reduction in the laminate can be measured using a conventional pulse-echo immersion UT approach by investigating the amplitude of the second and subsequent back-wall echoes. A "diffuse-field" technique may be developed from this principle, by observing the trailing backscatter noise from an insonified sample.

APPENDIX

MATLAB Scripts and Functions

```matlab
1  function T = crossc(wav1,wav2,wav_t,toffset)
2  % CROSSC Calculates the time difference between two peaks in a ...
       waveform using the
3  % offset of the cross-correlation function maximum
4  %
5  % INPUTS:
6  %      wav1(dim1), wav2(dim2): 1-D arrays containing waveform
7  %      amplitudes, where dim1 and dim2 are the number of sample points
8  %      for waveforms 1 and 2 respectively
9  %      wav_t(dim1): 1-D array containing time values for the waveform
10 %      (typically in microseconds)
11 %      toffset: time offset between the two peaks in microseconds
12 %
13 % OUTPUTS:
14 %      T: absolute scalar delta T value (in same units as wav_t)
15 %      corresponding to the offset of the maximum of the computed
16 %      cross-correlation function
17 %
18 % NOTE: wav1 and wav2 must be the same lengths, and although wav_t ...
       may have
19 % different ranges, the increment in time must be the same between ...
       the two
20 % A-scans (i.e., same sampling frequency).
21
22 if (numel(wav1) ~= numel(wav2))
23     fprintf('\nWaveform lengths must be the same.\n')
24     return
25 end
26
27 % Calculate cross-correlation by conjugate multiplication in frequency
28 % domain:
29 N = numel(wav1);
30 n = -(N-1):1:(N-1);
31 wav1_f = fft(wav1,2^nextpow2(2*N-1));
32 wav2_f = fft(wav2,2^nextpow2(2*N-1));
33
```

```
34  rxy = ifft(wav1_f.*conj(wav2_f));
35  rxy = [rxy(end-(N-1)+1:end);rxy(1:(N-1)+1)];
36
37  [rmax rind] = max(rxy);
38  if (n(rind) == 0) %CC function is maximum at zero offset (i.e., ...
        auto-correlation)
39      wavoff = 0;
40  elseif (n(rind) < 0)
41      wavoff = -(wav_t(1)-wav_t(1+abs(n(rind))));
42  else
43      wavoff = wav_t(1)-wav_t(1+n(rind));
44  end
45  T = toffset + wavoff;
46
47  end
```

```
1  function T = phase_delta(fft1,fft2,fs,toffset)
2  % PHASE_DELTA Calculate delta T between two peaks that corresponds ...
       to phase
3  % velocity
4  % INPUTS:
5  %        fft1(dim1): FFT of peak 1, where dim1 is the number of ...
       points in
6  %        the signal between fb <= f <= fe
7  %        fft2(dim1): FFT of peak 2
8  %        fs(dim1): frequency bandwidth
9  %        toffset: time offset between the two peaks in microseconds
10 % OUTPUTS:
11 %        T: absolute time difference between the two peaks in ...
       microseconds;
12
13 % Calculate max. frequency component for both waveforms
14 [fmax1 fmi1] = max(2*abs(fft1));
15 [fmax2 fmi2] = max(2*abs(fft2));
16
17 % Phase calculation and absolute phase values at central frequency
18 ph1 = unwrap2(angle(fft1(fmi1)));
19 ph2 = unwrap2(angle(fft2(fmi2)));
20
21 % Delta T calculation
22 T = toffset*10^-6 + (ph1/fs(fmi1))/(2*pi) - (ph2/fs(fmi2))/(2*pi);
23 T = T*10^6; %convert to microseconds
24
25 end
```

```matlab
1  function [ph] = unwrap2(ph)
2  %UNWRAP2 Unwraps the phase by +/- 2*pi at jumps of order greater ...
       than pi
3
4  numpts = numel(ph);
5
6  for i=2:numpts
7      if (ph(i)-ph(i-1) >  pi)
8          ph(i:end) = ph(i:end) - 2*pi;
9      elseif (ph(i)-ph(i-1) < -pi)
10          ph(i:end) = ph(i:end) + 2*pi;
11      end
12  end
13
14  end
```

```matlab
1  %pixelcount.m
2  %
3  % Ajith Subramanian, Last Updated: 3/21/13
4  %
5  % Description:  Reads raw image data from *.vol file using format
6  % specifications in *.vgi file.  Binarizes data based user input for
7  % threshold range and counts the number of pixels corresponding to the
8  % threshold range (i.e., "microcrack pixels").  The script assumes ...
       that the
9  % *.vol file data is ordered the following way w.r.t to sample geometry:
10  % width -> thickness -> length
11  %
12  % NOTE:  Only single slices are loaded into memory
13
14  clear all; close all; fclose all; clc
15
16                   %-----------------------------------%
17                   %     Open *.vol and *.vgi files    %
18                   %-----------------------------------%
19
20  [vol_filename vol_pathname] = uigetfile('*.vol','Choose *.vol file');
21  [vgi_filename vgi_pathname] = uigetfile('*.vgi','Choose *.vgi file');
22  if (vol_filename == 0) | (vgi_filename == 0)
23      clear all; close all; fclose all; clc
24      return
25  end
26  addpath(vol_pathname); addpath(vgi_pathname)
27
28  fidvol = fopen(vol_filename,'r','l');
29  fidvgi = fopen(vgi_filename,'r','l');
30
31  % Determine .vol file size
32  fseek(fidvol,0,'eof');
33  vol_filesize = ftell(fidvol);
```

```matlab
34  frewind(fidvol);
35
36  % Get size from .vgi file
37  fgetl(fidvgi); fgetl(fidvgi); %Skip first two lines
38  size = fscanf(fidvgi,'size = %f %f %f');
39  xlim = size(1); ylim = size(2); zlim = size(3);
40
41                   %-----------------------------------%
42                   %                 Inputs            %
43                   %-----------------------------------%
44
45  % number of slices to skip between reads, i.e. numskip = 9 will read ...
        every
46  % 10th slice:
47  numskip = 9;
48  % Number of slices used to calculate thresholded pixels per volume ...
        (percentage)
49  numsvol = 10;
50  % Upper and lower bounds of threshold:
51  tlo = 20;
52  thi = 26.0;
53  % Set offset to first slice (# of slices) and range
54  numoffset = 157;
55  zrange = 1844; % choose z limit slice for reading
56
57                   %-----------------------------------%
58                   %          Read and Process Data    %
59                   %-----------------------------------%
60
61  numslices = zrange-numoffset;
62  fseek(fidvol,numoffset*xlim*ylim*4,'bof');
63  pos = ftell(fidvol);
64  m=1;
65  while (pos <= zrange*xlim*ylim*4)
66      dat = fread(fidvol,xlim*ylim,'single');
67      dat = cast(dat,'single');
68      slice = reshape(dat,xlim,ylim);
69      thresh = (slice > tlo) & (slice < thi);
70      numpix(m) = numel(nonzeros(thresh)); %Not initialized
71      clear dat; clear slice; clear thresh;
72      m = m+1;
73      fseek(fidvol,numskip*xlim*ylim*4,'cof'); %Skip 'numskip' amount ...
            of slices
74      pos = ftell(fidvol);
75  end
76  % Flip to express data backwards
77  numpix = fliplr(numpix);
78  pernumpix = (numpix/(xlim*ylim))*100; % percentage of thresh. pixels ...
        per slice
79  totpix = sum(numpix);
80  % Percentage of thresh. pixels in volume given by ...
        xlim*ylim*numslices where
81  %numslices = zrange - numoffset
```

```matlab
82  pertotpix = (totpix/(xlim*ylim*numel(numpix)))*100;
83  dist = linspace(0,numel(pernumpix-1)*0.0143,numel(pernumpix));
84
85  pts = 0;
86  n=1;
87  while (pts < numslices)
88      if (pts+numsvol > numel(numpix))
89          tpix = sum(numpix(pts+1:end));
90          pertpix(n) = tpix/(xlim*ylim*(numel(numpix)-pts+1))*100;
91          break
92      end
93      tpix = sum(numpix(pts+1:pts+numsvol));
94      pertpix(n) = tpix/(xlim*ylim*numsvol)*100;
95      pts = pts+numsvol;
96      n = n+1;
97  end
98
99                  %------------------------------------%
100                 %                 Output             %
101                 %------------------------------------%
102
103 fprintf('%% thresholded pixels per volume: %f\n',pertotpix)
104 save(vol_filename(1:end-4),'numpix','pernumpix','pertotpix');
105
106                 %------------------------------------%
107                 %                 Plot               %
108                 %------------------------------------%
109
110 figure;
111 plot(dist,pernumpix,'.')
112 title('% Thresholded Pixels Per Slice; (thresholded pixels)/(total ...
        pixels in slice)*100%')
113 ylabel('% Thresholded Pixels Per Slice')
114 xlabel('Points')
115
116 figure;
117 plot(pertpix,'.')
118 title('% Thresholded Pixels Per Volume; (thresholded pixels)/(total ...
        pixels in volume)*100%')
119 ylabel('% Thresholded Pixels Per Volume')
120 xlabel('Points')
121 %
122 % x = linspace(0,xlim-1,1);
123 % y = linspace(0,ylim-1,1);
124 % image(x,y,slice','CDataMapping','scaled');
125 % set(gca,'DataAspectRatio',[1 1 1])
126 % colormap(gray)
127 %
128
129 fclose all;
130 rmpath(vol_pathname); rmpath(vgi_pathname);
```

```matlab
1  function [C,S] = stiffness(E1,E2,E3,G12,G13,G23,nu12,nu13,nu23)
2  % STIFFNESS Calculate single-ply properties
3
4  nu21 = (E2/E1)*nu12;
5  nu31 = (E3/E1)*nu13;
6  nu32 = (E3/E2)*nu23;
7
8  %Create compliance and stiffness matrices
9  S = [1/E1 -nu21/E2 -nu31/E3 0 0 0; ...
10       -nu12/E1 1/E2 -nu32/E3 0 0 0; ...
11       -nu13/E1 -nu23/E2 1/E3 0 0 0; ...
12       0 0 0 1/G23 0 0; ...
13       0 0 0 0 1/G13 0; ...
14       0 0 0 0 0 1/G12];
15  C = inv(S);
16
17  % The following is for checking if the inverted C matrix is the ...
       same as
18  % the one calculated using the Jones book formulas
19  d = (1-nu12*nu21-nu23*nu32-nu31*nu13-2*nu21*nu32*nu13)/(E1*E2*E3);
20  C2 = [(1-nu23*nu32)/(E2*E3*d) (nu12+nu32*nu13)/(E1*E3*d) ...
       (nu13+nu12*nu23)/(E1*E2*d) 0 0 0; ...
21        (nu12+nu32*nu13)/(E1*E3*d) (1-nu13*nu31)/(E1*E3*d) ...
            (nu23+nu21*nu13)/(E1*E2*d) 0 0 0; ...
22        (nu13+nu12*nu23)/(E1*E2*d) (nu23+nu21*nu13)/(E1*E2*d) ...
            (1-nu12*nu21)/(E1*E2*d) 0 0 0; ...
23        0 0 0 G23 0 0; 0 0 0 0 G13 0; 0 0 0 0 0 G12];
24
25  % plane stress reduced constants
26  C11 = E1/(1-nu12/nu21);
27  C12 = nu12*E2/(1-nu12*nu21);
28  C22 = E2/(1-nu12*nu21);
29  C66 = G12;
30  end
```

```matlab
1  function [T,Ct,St] = transformation(C,theta)
2  % TRANSFORMATION Transform coordinate system given stiffness matrix
3  % and angle of rotation
4
5  % Theta is in radians
6
7  % transformation matrix
8  T = [cos(theta)*cos(theta) sin(theta)*sin(theta) 0 0 0 ...
       -sin(2*theta); ...
9        sin(theta)*sin(theta) cos(theta)*cos(theta) 0 0 0 sin(2*theta); ...
10       0 0 1 0 0 0 ; ...
11       0 0 0 cos(theta) sin(theta) 0; ...
12       0 0 0 -sin(theta) cos(theta) 0; ...
13       sin(theta)*cos(theta) -sin(theta)*cos(theta) 0 0 0 ...
            cos(theta)*cos(theta)-sin(theta)*sin(theta)];
```

```
14
15  Ct = T*C*T';
16  St = inv(Ct);
17  end
```

```
1   function [V,m1_0,m3_0,T0,W0,p] = incwaveprop(Ct,n1,n2,n3,dens)
2   % INCWAVEPROP Calculate properties of incident longitudinal wave given
3   % material properties and propagation direction
4
5   % Characteristic equation in terms of phase velocity (alpha = rho*V^2)
6   G = zeros(3,3);
7   G(1,1) = Ct(1,1)*n1*n1 + Ct(6,6)*n2*n2 + Ct(5,5)*n3*n3;
8   G(1,2) = (Ct(1,2) + Ct(6,6))*n1*n2;
9   G(1,3) = (Ct(1,3) + Ct(5,5))*n1*n3;
10  G(2,1) = G(1,2);
11  G(2,2) = Ct(6,6)*n1*n1 + Ct(2,2)*n2*n2 + Ct(4,4)*n3*n3;
12  G(2,3) = (Ct(2,3) + Ct(4,4))*n2*n3;
13  G(3,1) = G(1,3);
14  G(3,2) = G(2,3);
15  G(3,3) = Ct(5,5)*n1*n1 + Ct(4,4)*n2*n2 + Ct(3,3)*n3*n3;
16  % Equation coeff:
17  a = -(G(1,1) + G(2,2) + G(3,3));
18  b = -(G(1,2)*G(1,2) + G(1,3)*G(1,3) + G(2,3)*G(2,3) - G(1,1)*G(2,2) ...
        - ...
19      G(1,1)*G(3,3) - G(2,2)*G(3,3));
20  c = -(G(1,1)*G(2,2)*G(3,3) + 2*G(1,2)*G(1,3)*G(2,3) - ...
      G(1,1)*G(2,3)*G(2,3) - ...
21      G(2,2)*G(1,3)*G(1,3) - G(3,3)*G(1,2)*G(1,2));
22  % syms alpha; % alpha is equal to rho*V^2; m3_0 is unknown vertical
23              % of slowness
24  % eq = alpha^3 + a*alpha^2 + b*alpha + c;
25  sol = eval(solve('x^3 + a*x^2 + b*x + c','x'));
26  solr = real(sol); soli = imag(sol);
27  V = sort(sqrt(solr/dens),'descend');
28
29  % Slowness of longitudinal wave
30  m1_0 = n1/V(1); m3_0 = n3/V(1);
31
32  T0 = zeros(3,3);
33  T0(1,1) = Ct(1,1)*m1_0*m1_0 + (Ct(5,1)+Ct(1,5))*m3_0*m1_0 + ...
      Ct(5,5)*m3_0*m3_0 - dens;
34  T0(1,2) = Ct(1,6)*m1_0*m1_0 + (Ct(5,6)+Ct(1,4))*m3_0*m1_0 + ...
      Ct(5,4)*m3_0*m3_0;
35  T0(1,3) = Ct(1,5)*m1_0*m1_0 + (Ct(5,5)+Ct(1,3))*m3_0*m1_0 + ...
      Ct(5,3)*m3_0*m3_0;
36  T0(2,1) = T0(1,2);
37  T0(2,2) = Ct(6,6)*m1_0*m1_0 + (Ct(4,6)+Ct(6,4))*m3_0*m1_0 + ...
      Ct(4,4)*m3_0*m3_0 - dens;
38  T0(2,3) = Ct(6,5)*m1_0*m1_0 + (Ct(4,5)+Ct(6,3))*m3_0*m1_0 + ...
      Ct(4,3)*m3_0*m3_0;
39  T0(3,1) = T0(1,3);
```

```matlab
40  T0(3,2) = T0(2,3);
41  T0(3,3) = Ct(5,5)*m1_0*m1_0 + (Ct(3,5)+Ct(5,3))*m3_0*m1_0 + ...
        Ct(3,3)*m3_0*m3_0 - dens;
42  W0(1,1) = T0(2,2)*T0(3,3) - T0(3,2)*T0(2,3);
43  W0(1,2) = T0(2,3)*T0(3,1) - T0(2,1)*T0(3,3);
44  W0(1,3) = T0(1,2)*T0(2,3) - T0(1,3)*T0(2,2);
45  W0(2,1) = W0(1,2);
46  W0(2,2) = T0(3,3)*T0(1,1) - T0(1,3)*T0(3,1);
47  W0(2,3) = T0(3,1)*T0(1,2) - T0(3,2)*T0(1,1);
48  W0(3,1) = W0(1,3);
49  W0(3,2) = W0(2,3);
50  W0(3,3) = T0(1,1)*T0(2,2) - T0(2,1)*T0(1,2);
51
52  [Wmax Wind] = max(diag(W0));
53  p = zeros(3,1);
54  if (Wind == 1)
55      p(1) = sqrt(max(diag(W0))/sum(diag(W0)));
56      p(2) = (1/p(1))*(W0(2,1))/sum(diag(W0));
57      p(3) = (1/p(1))*(W0(3,1))/sum(diag(W0));
58  elseif (Wind == 2)
59      p(2) = sqrt(max(diag(W0))/sum(diag(W0)));
60      p(1) = (1/p(2))*(W0(1,2))/sum(diag(W0));
61      p(3) = (1/p(2))*(W0(3,2))/sum(diag(W0));
62  else
63      p(3) = sqrt(max(diag(W0))/sum(diag(W0)));
64      p(1) = (1/p(3))*(W0(1,3))/sum(diag(W0));
65      p(2) = (1/p(3))*(W0(2,3))/sum(diag(W0));
66  end
67
68  end
```

```matlab
1  function [Vg3_refl,V_refl,p_refl,m3_refl,n3_refl,n1_refl] = ...
       ref(Ct,m1_0,dens)
2  %REF Calculates reflected/refracted wave properties (longitudinal wave)
3
4  % Characteristic equation (Christoffel matrix)
5  T = sym(zeros(3,3)); syms m3
6  T(1,1) = vpa(Ct(1,1)*m1_0*m1_0 + (Ct(5,1)+Ct(1,5))*m3*m1_0 + ...
       Ct(5,5)*m3*m3 - dens);
7  T(1,2) = vpa(Ct(1,6)*m1_0*m1_0 + (Ct(5,6)+Ct(1,4))*m3*m1_0 + ...
       Ct(5,4)*m3*m3);
8  T(1,3) = vpa(Ct(1,5)*m1_0*m1_0 + (Ct(5,5)+Ct(1,3))*m3*m1_0 + ...
       Ct(5,3)*m3*m3);
9  T(2,1) = T(1,2);
10 T(2,2) = vpa(Ct(6,6)*m1_0*m1_0 + (Ct(4,6)+Ct(6,4))*m3*m1_0 + ...
       Ct(4,4)*m3*m3 - dens);
11 T(2,3) = vpa(Ct(6,5)*m1_0*m1_0 + (Ct(4,5)+Ct(6,3))*m3*m1_0 + ...
       Ct(4,3)*m3*m3);
12 T(3,1) = T(1,3);
13 T(3,2) = T(2,3);
14 T(3,3) = vpa(Ct(5,5)*m1_0*m1_0 + (Ct(3,5)+Ct(5,3))*m3*m1_0 + ...
```

```
           Ct(3,3)*m3*m3 - dens);
15
16    % Solve for 6 solutions in m3
17  sol2 = solve(det(T));
18
19  % m3:
20  m3val = double(sol2);
21
22  n3ref = m3val./sqrt(m1_0^2 + m3val.^2);
23  n1ref = sqrt(1 - n3ref.^2);
24  Vrefval = n3ref./double(m3val);
25
26  % For each real solution in m3, calculate the normal component of group
27  % velocity to determine reflected and refracted waves
28  p = zeros(3,6);
29  Vg3 = zeros(6,1);
30  V_refl = zeros(3,1);
31  m_refl = zeros(3,1);
32  p_refl = zeros(3,3);
33  Vg3_refl = zeros(3,1);
34  for m=1:6
35      m_3 = m3val(m);
36      % Substitute slowness value of reflected longitudinal wave into
37      % Chrstoffel matrix:
38      T2 = double(subs(T,m3,m3val(m)));
39
40      W = zeros(3,3);
41      % Adjugate to the Christoffel matrix:
42      W(1,1) = T2(2,2)*T2(3,3) - T2(3,2)*T2(2,3);
43      W(1,2) = T2(2,3)*T2(3,1) - T2(2,1)*T2(3,3);
44      W(1,3) = T2(1,2)*T2(2,3) - T2(1,3)*T2(2,2);
45      W(2,1) = W(1,2);
46      W(2,2) = T2(3,3)*T2(1,1) - T2(1,3)*T2(3,1);
47      W(2,3) = T2(3,1)*T2(1,2) - T2(3,2)*T2(1,1);
48      W(3,1) = W(1,3);
49      W(3,2) = W(2,3);
50      W(3,3) = T2(1,1)*T2(2,2) - T2(2,1)*T2(1,2);
51
52      % Calculate polarization vectors
53      [Wmax Wind] = max(diag(W));
54      if (Wind == 1)
55          p(1,m) = sqrt(max(diag(W))/sum(diag(W)));
56          p(2,m) = (1/p(1,m))*(W(2,1))/sum(diag(W));
57          p(3,m) = (1/p(1,m))*(W(3,1))/sum(diag(W));
58      elseif (Wind == 2)
59          p(2,m) = sqrt(max(diag(W))/sum(diag(W)));
60          p(1,m) = (1/p(2,m))*(W(1,2))/sum(diag(W));
61          p(3,m) = (1/p(2,m))*(W(3,2))/sum(diag(W));
62      else
63          p(3,m) = sqrt(max(diag(W))/sum(diag(W)));
64          p(1,m) = (1/p(3,m))*(W(1,3))/sum(diag(W));
65          p(2,m) = (1/p(3,m))*(W(2,3))/sum(diag(W));
66      end
```

```
67
68       Vg3(m) = (1/dens)*((Ct(5,1)*m1_0 + Ct(5,5)*m_3)*p(1,m)^2 + ...
69              (Ct(4,6)*m1_0 + Ct(4,4)*m_3)*p(2,m)^2 + ...
70              (Ct(3,5)*m1_0 + Ct(3,3)*m_3)*p(3,m)^2 + ...
71              ((Ct(4,1) + Ct(5,6))*m1_0 + (Ct(4,5) + ...
                   Ct(5,4))*m_3)*p(1,m)*p(2,m) + ...
72              ((Ct(3,6) + Ct(4,5))*m1_0 + (Ct(3,4) + ...
                   Ct(4,3))*m_3)*p(3,m)*p(2,m) + ...
73              ((Ct(3,1) + Ct(5,5))*m1_0 + (Ct(3,5) + ...
                   Ct(5,3))*m_3)*p(1,m)*p(3,m));
74 end
75
76 Vref = max(Vrefval);
77 rind = find(Vg3 > 0 | imag(Vg3) < 0); % Find positive normal group ...
      velocity components
78                                       % or Vg3 whose imaginary ...
                                           components
79                                       % are negative
80 Vg3_refl = Vg3(rind);
81 V_refl = Vrefval(rind);
82 p_refl = p(:,rind);
83 m3_refl = m3val(rind);
84 n3_refl = m3_refl./sqrt(m1_0^2 + m3_refl.^2);
85 n1_refl = sqrt(1 - n3_refl.^2);
86
87 % Resort so that longitudinal reflected wave is first
88 [V_refl sortind] = sort(V_refl,'descend');
89 p_refl = p_refl(:,sortind);
90 m3_refl = m3_refl(sortind);
91 n3_refl = n3_refl(sortind);
92 n1_refl = n1_refl(sortind);
93
94 end
```

BIBLIOGRAPHY

[1] V. K. Kinra and V. Dayal, "Ultrasonic nondestructive evaluation of fibre-reinforced composite materials - a review," *Sadhana*, vol. 11, no. 3, pp. 419–432, 1987.

[2] S. Baste, R. El Guerjouma, and B. Audoin, "Effect of microcracking on the macroscopic behaviour of ceramic matrix composites: ultrasonic evaluation of anisotropic damage," *Mechanics of Materials*, vol. 14, no. 1, pp. 15–31, 1992.

[3] U. Polimeno, M. Meo, D. Almond, and S. Angioni, "Detecting low velocity impact damage in composite plate using nonlinear acoustic/ultrasound methods," *Applied Composite Materials*, vol. 17, no. 5, pp. 481–488, 2010.

[4] H. P. Kong, Z. Zhang, and L. F. Li, "Factors influencing acousto-ultrasonic approach to impact damage in composite materials," *Advanced Materials Research*, vol. 393, pp. 97–101, 2012.

[5] J. A. Nairn, "Matrix microcracking in composites," *Polymer Matrix Composites*, vol. 2, pp. 403–432, 2000.

[6] J. Nairn and S. Hu, "The initiation and growth of delaminations induced by matrix microcracks in laminated composites," *International Journal of Fracture*, vol. 57, no. 1, pp. 1–24, 1992.

[7] J. A. Nairn, "Microcracking, microcrack-induced delamination, and longitudinal splitting of advanced composite structures," *Final Report Utah Univ., Salt Lake City. Dept. of Materials Science and Engineering.*, vol. 1, 1992.

[8] R. Olsson, M. V. Donadon, and B. G. Falzon, "Delamination threshold load for dynamic impact on plates," *International Journal of Solids and Structures*, vol. 43, no. 10, pp. 3124–3141, 2006.

[9] G. Davies and X. Zhang, "Impact damage prediction in carbon composite structures," *International Journal of Impact Engineering*, vol. 16, no. 1, pp. 149–170, 1995.

[10] G. Schoeppner and S. Abrate, "Delamination threshold loads for low velocity impact on composite laminates," *Composites Part A: Applied Science and Manufacturing*, vol. 31, no. 9, pp. 903–915, 2000.

[11] D. Cartie and P. Irving, "Effect of resin and fibre properties on impact and compression after impact performance of CFRP," *Composites Part A: Applied Science and Manufacturing*, vol. 33, no. 4, pp. 483–493, 2002.

[12] H. Yan, C. Oskay, A. Krishnan, and L. R. Xu, "Compression-after-impact response of woven fiber-reinforced composites," *Composites Science and Technology*, vol. 70, no. 14, pp. 2128–2136, 2010.

[13] V. Dayal and V. K. Kinra, "Leaky lamb waves in an anisotropic plate. ii: Nondestructive evaluation of matrix cracks in fiber-reinforced composites," *The Journal of the Acoustical Society of America*, vol. 89, p. 1590, 1991.

[14] M. D. Seale, B. T. Smith, and W. Prosser, "Lamb wave assessment of fatigue and thermal damage in composites," *The Journal of the Acoustical Society of America*, vol. 103, p. 2416, 1998.

[15] D. Hull, H. Kautz, and A. Vary, "Measurement of ultrasonic velocity using phase-slope and cross-correlation methods," *Materials Evaluation*, vol. 43, no. 11, pp. 1455–1460, 1985.

[16] S. J. Orfanidis, *Optimum Signal Processing: An Introduction*. Macmillan New York, 1985.

[17] K. Maslov, R. Y. Kim, V. K. Kinra, and N. J. Pagano, "A new technique for the ultrasonic detection of internal transverse cracks in carbon-fibre/bismaleimide composite laminates," *Composites Science and Technology*, vol. 60, no. 12, pp. 2185–2190, 2000.

[18] V. K. Kinra, A. S. Ganpatye, and K. Maslov, "Ultrasonic ply-by-ply detection of matrix cracks in laminated composites," *Journal of Nondestructive Evaluation*, vol. 25, no. 1, pp. 37–49, 2006.

[19] A. H. Nayfeh, *Wave Propagation in Layered Anisotropic Media*. North-Holland Amsterdam, 1995.

[20] D. Chimenti, S. Rokhlin, and P. Nagy, *Physical Ultrasonics of Composites*. OUP USA, 2011.

[21] J. N. Reddy, *Mechanics of Laminated Composite Plates and Shells: Theory and Analysis*. CRC, 2003.

[22] S. Rokhlin, T. Bolland, and L. Adler, "Reflection and refraction of elastic waves on a plane interface between two generally anisotropic media," *The Journal of the Acoustical Society of America*, vol. 79, p. 906, 1986.

[23] B. A. Auld, *Acoustic Fields and Waves in Solids*. RE Krieger, 1990.

[24] C.-T. Ng and M. Veidt, "Scattering analysis of fundamental anti-symmetric lamb wave at delaminations in composite laminates," in *6th Australasian Congress on Applied Mechanics (ACAM 6)*, pp. 860–867, Engineers Australia, 2010.

[25] C. Ramadas, K. Balasubramaniam, M. Joshi, and C. Krishnamurthy, "Interaction of guided lamb waves with an asymmetrically located delamination in a laminated composite plate," *Smart Materials and Structures*, vol. 19, no. 6, p. 065009, 2010.